RSC Advances

PAPER

View Article Online
View Journal | View Issue

Open Access Article. Published on 31 October 2023. Downloaded on 10/24/2025 6:18:49 PM.
This article is licensed under a Creative Commons Attribution-NonCommercial 3.0 Unported Licence.

Check for updates

Cite this: *RSC Adv.*, 2023, **13**, 31908

Novel quinoxaline-3-propanamides as VGFR-2 inhibitors and apoptosis inducers†

Magda M. F. Ismail,[a] Taghreed Z. Shawer,[a] Rabab S. Ibrahim,[a] Mostafa S. Abusaif,[b] Mona M. Kamal,[c] Rasha M. Allam[d] and Yousry A. Ammar[b]

Vascular endothelial growth factor receptor-2 is a vital target for therapeutic mediation in various types of cancer. This study was aimed at exploring the cytotoxic activity of seventeen novel quinoxaline-3-propanamides against colon cancer (HCT-116) and breast cancer (MCF-7) using MTT assay. Results revealed that compounds 8, 9, and 14 elicited higher cytotoxicity than the reference drugs, doxorubicin (DOX) and sorafenib. Interestingly, they are more selective for HCT-116 (SI 11.98–19.97) and MCF-7 (SI 12.44–23.87) compared to DOX (SI HCT-116 0.72 and MCF-7 0.9). These compounds effectively reduced vascular endothelial growth factor receptor-2; among them, compound **14** displayed similar VEGFR-2 inhibitory activity to sorafenib (IC_{50} 0.076 M). The ability of **14** to inhibit angiogenesis was demonstrated by a reduction in VEGF-A level compared to control. Furthermore, it induced a significant increase in the percentage of cells at pre-G1 phase by almost 1.38 folds (which could be indicative of apoptosis) and an increase in G2/M by 3.59 folds compared to the control experiment. A flow cytometry assay revealed that compound **14** triggered apoptosis *via* the programmed cell death and necrotic pathways. Besides, it caused a remarkable increase in apoptotic markers, *i.e.*, caspase-3 p53 and BAX. When compared to the control, significant increase in the expression levels of caspase-3 from 47.88 to 423.10 and p53 from 22.19 to 345.83 pg per ml in MCF-7 cells. As well, it increased the proapoptotic protein BAX by 4.3 times while lowering the antiapoptotic marker BCL2 by 0.45 fold. Docking studies further supported the mechanism, where compound **14** showed good binding to the essential amino acids in the active site of VEGFR-2. Pharmacokinetic properties showed the privilege of these hits over sunitinib: they are not substrates of P-gp protein; this suggests that they have less chance to efflux out of the cell, committing maximum effect; and in addition, they do not allow permeation to the BBB.

Received 26th July 2023
Accepted 23rd September 2023

DOI: 10.1039/d3ra05066a

rsc.li/rsc-advances

1. Introduction

One may argue that abnormal angiogenesis is a crucial condition for the growth and spread of tumors. The growth and occurrence of numerous tumor types are strongly correlated with the aberrant expression of VEGFR-2 in neovascular tumor endothelial cells, according to mounting evidence.[1,2] At the moment, blocking VEGFRs to target tumor angiogenesis is a successful oncotherapy method.[3–5] All VEGFR-2 inhibitors, despite the fact that the majority of them lack specificity, provide differing degrees of therapeutic efficacy against various tumor types by inhibiting angiogenesis and lymphangiogenesis.[6] Currently, there are three types of VEGFR inhibitors: type I inhibitors, type II inhibitors, and type III inhibitors.[7] Sunitinib (SU11248), a type I inhibitor, is the first small molecule to contain the indolin-2-one template and is effective against a number of kinases, including the stem cell factor receptor (c-Kit), platelet-derived growth factor receptors A and B (PDGFRA and PDGFRB), colony-stimulating factor 1 receptor (CSF-1R), FMS-like tyrosine kinase 3. (FLT3)[8] Type II inhibitors, *e.g.*, sorafenib, are characterized by binding to the inactive "DFG-out" conformation of the kinase and occupying a hydrophobic pocket adjacent to the ATP-binding site.[9,10] Structurally, the extension into the less conservative allosteric hydrophobic back pocket facilitates the affinity and selectivity of the type II inhibitors.[11] Type III, *e.g.*, vatalanib, could exert their pharmacological functions by irreversibly binding to cysteine at specific sites on the kinases.[12]

Quinoxaline derivatives are a widespread class of heterocycles receiving the most attention, especially in the field of chemotherapy.[13–16] Many drugs incorporating the quinoxaline

[a]Department of Pharmaceutical Medicinal Chemistry and Drug Design, Faculty of Pharmacy (Girls), Al-Azhar University, Cairo, 11754, Egypt. E-mail: m.elalfy101@gmail.com; magdaismail@azhar.edu.eg

[b]Department of Chemistry, Faculty of Science, Al-Azhar University, Cairo, 11754, Egypt

[c]Department of Pharmacology, Faculty of Pharmacy (Girls), 11754 Al-Azhar University, Cairo, Egypt

[d]Department of Pharmacology, Medical and Clinical Research Institute, National Research Centre, 12622, Dokki, Cairo, Egypt

† Electronic supplementary information (ESI) available. See DOI: https://doi.org/10.1039/d3ra05066a

© 2023 The Author(s). Published by the Royal Society of Chemistry

Open Access Article. Published on 31 October 2023. Downloaded on 10/24/2025 6:18:49 PM.
This article is licensed under a Creative Commons Attribution-NonCommercial 3.0 Unported Licence.

scaffold have achieved promising results and have been submitted to clinical trials for anticancer therapeutic purposes.[17,18]

The therapeutic applicability of current VEGFR inhibitors, however, is constrained to some extent by their low clinical efficacy and probable toxicity. Based on the aforementioned findings (*cf.* Fig. 1) and as a continuation of our prior work in the field of the design and synthesis of new anticancer medicines,[19–26] a new series of 6-chloroquinoxaline-3-propanamides have been designed as sunitinib's mimetic to optimize pharmacodynamics properties and to overcome certain pharmacokinetic problems demonstrated on sunitinib clinical use such as, BBB permeation and being P-gp substrate.

Herein, the hetero-aromatic system was designed to be 6-chloroquinoxalin-2-one as an isostere for 5-fluoroindoline-2-one, and the linker group was an aliphatic chain ($-CH_2CH_2-$) as a chain contraction to replace 2,4-dimethyl-1*H*-pyrrole of sunitinib. The pharmacophore moiety was kept in all the designed compounds as an amide group. The terminal hydrophobic moiety was an aryl moiety with a variation of substituents instead of an aliphatic amino side chain of sunitinib. These modifications were followed to optimize both the pharmacodynamics and pharmacokinetic criteria of sunitinib, (Fig. 1).

2. Discussion

2.1. Chemistry

The starting material, **3**,[27] was readily produced in nearly a quantitative yield (95%) by cyclocondensing 4-chloro-1,2-phenylenediamine, **1**, with ketoglutaric acid, **2**, in acetic acid/ethanol with stirring at room temperature. The acid derivative **3** was then treated with methanol and a few drops of concentrated H_2SO_4 in a reflux environment for three hours (Scheme 1) to produce the equivalent methyl ester **4**.[27]

Additionally, aminolysis[28] of ethyl propanoate ester **4** with substituted anilines at positions 2, 3, or 4 was carried out to yield the corresponding quinoxaline-3-propanamides **5–17**. A single molecule of methanol was eliminated through reflux in a catalytic amount of DMF in ethanol solvent over the course of eight to sixteen hours, successfully completing the reaction despite aniline's very weak nucleophilicity towards the carbonyl carbon of the ester group, (Scheme 1).

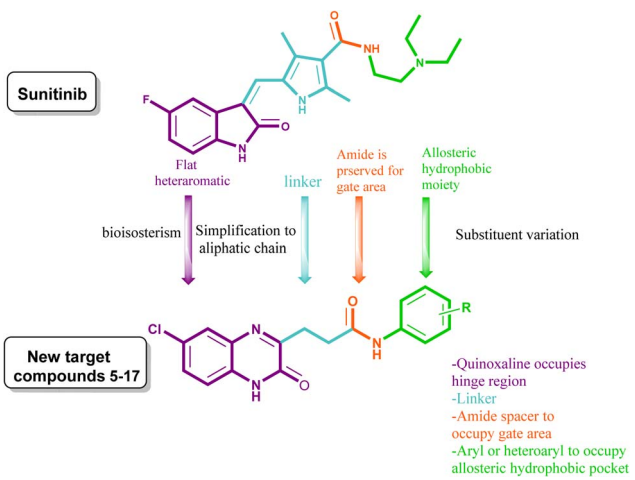

Fig. 1 Feauture similarities between ligand and target compounds.

The spectroscopic and micro-analytical data from all quinoxaline-3-propanamides **5–17** were used to elucidate them. All of our series are characterized by the presence of two triplets in the ^{1}H NMR spectra that indicate linker protons ($-CH_2-CH_2-CO$) at δ (ppm): 1.63–1.75 for CH_2 and 2.25–2.38 for CH_2CO protons. Besides, deshielded signals for three quinox-Hs and four aryl-Hs are appeared at their appropriate aromatic region. It is important to note several distinctive signals in the ^{1}H NMR spectra of our series; for example, the 4-CH_3 protons of compound **11** appeared as a singlet at around δ 2.40 ppm, while the 4-OCH_3 protons of compound **14** appeared at about δ 3.90 ppm. Compound **15**'s ^{1}H NMR spectrum showed a singlet signal at about δ 2.67 ppm that was attributed to $COCH_3$ protons. In the ^{1}H NMR spectrum of the ethyl ester **17**, a triplet–quartet pattern was seen at δ 1.34 and 4.36 ppm respectively.

Hydrazinolysis of the ester **4** with hydrazine hydrate using absolute ethanol produced a good yield of the corresponding acid hydrazide derivative, **18**.[29] Nucleophilic substitution reaction of compound **18** with 2,4-dichlorobenzoyl chloride was achieved by heating under reflux condition in ethanol with DMF drops[30] to furnish the corresponding 2,4-dichlorobenzoyl hydrazide, **19** (Scheme 2). Furthermore, synthesis of the target compounds **20** and **21** was achieved by treatment of the intermediate **18** with the appropriate acid anhydrides namely; succinic anhydride or phthalic anhydride respectively *via* ring opening amidation reaction in ethanol with catalytic amount of DMF.[31] Compound **20** was verified based on spectral data; its IR spectrum displayed extra bands at 3360 and 1706 cm^{-1} contributed to OH and C=O of carboxyl group respectively. ^{1}H NMR spectrum displayed extra two triplets at δ 2.38 and 2.59 ppm contributed to CH_2CH_2 protons of succinic acid moiety. As mentioned in literature,[32] reaction of the starting material **18** with phthalic anhydride is a solvent dependent. Thus, when the reaction was carried out in ethanol; the product was formulated as carboxylic acid derivative **21**. While performing the reaction in glacial acetic acid as a solvent, the corresponding isoindoline derivative **22** was obtained *via* ring closure due to condensation reaction. The isoindoline **22** was further confirmed by refluxing compound **21** in glacial acetic for 2 h to afford one and the same product (**22**). The structures of these compounds were consistent with spectral analysis. IR of compound **21** showed stretching bands around 3339 and 1705 cm^{-1} pointing to hydroxyl and carbonyl of CO*OH* respectively. ^{1}H NMR spectrum showed a characteristic singlet at δ 10.80 ppm attributed to carboxylic proton; also 4 extra signals (4 Ar–H) at the range from δ 7.44 to 8.74 ppm were observed. Mass spectrum exhibited a peak at *m*/*z* 414 referred to molecular ion peak (M+). Concerning IR spectrum of compound **22**, lack of broad band of OH and NH is observed due to removal of water molecule. In addition, the frequency of carbonyl band is increased due to ring closure, where ^{1}H NMR spectrum displayed only two signals at 12.22 and 12.54 ppm for two NH

Open Access Article. Published on 31 October 2023. Downloaded on 10/24/2025 6:18:49 PM.
This article is licensed under a Creative Commons Attribution-NonCommercial 3.0 Unported Licence.

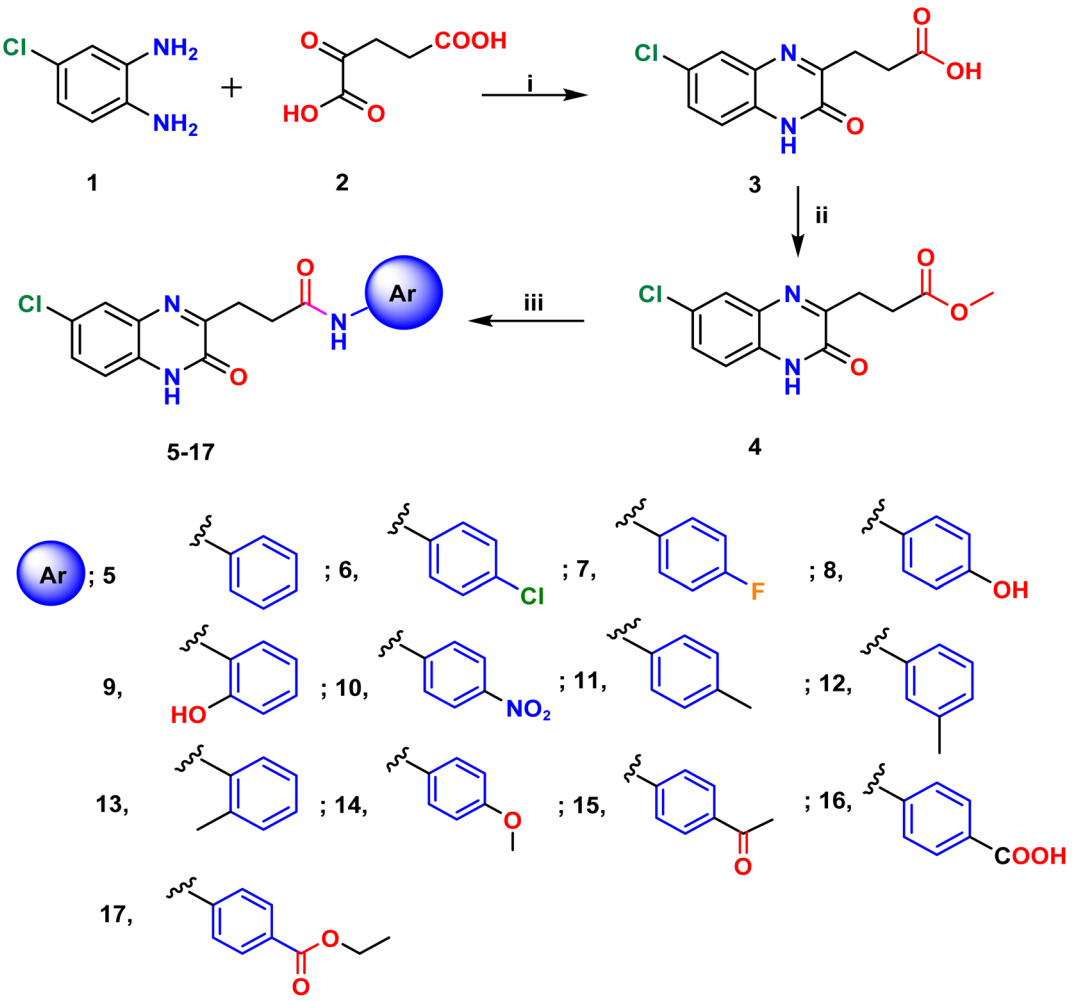

Scheme 1 Reagents and conditions, (i) acetic acid/EtOH, stirr, r.t. 15 min (ii) CHsOH, dps conc. H_2SO_4, reflux, 3 h, (iii) aromatic amines, EtOH/DMF, reflux, 8–16 h.

protons with lack of CO*OH* and one NH signals ensures the cyclization (Scheme 2).

2.2. Biological evaluation

2.2.1 Cytotoxic activity of the new compounds against human tumor cells. The potential antitumor activity of the synthesized compounds was investigated against HCT-116 and MCF-7 using the MTT assay.[33] The IC_{50} values of the new derivatives against the aforementioned cancer cell lines are presented in Table 1. Clearly, results for all chemicals on both cell lines are generally comparable, but MCF-7 was more responsive to our hits than HCT-116. We can realize that the anticancer activity is greatly affected by the lipophilicity and capability for H bonding with the receptor. The IC_{50} of **8** (4-OH) is 4.72 μM for HCT116 and 3.95 μM for MCF-7; these results are comparable to those of sunitinib,[34,35] and highly potent than those of sorafenib,[36] (*c.f.* Table 2). The slightly more lipophilic compound **14** (4-OCH_3, IC_{50} 5.81, 4.61 μM) elicited enhanced activity against HCT116 and MCF-7 cell lines, respectively. The more lipophilic bioisostere **11**, (4-CH_3), however, showed low IC_{50} values of 61.35 μM for the HCT116 cell line and 53.95 μM for the MCF-7 cell line. Notably, when examining the electronic effect on the activity, the electron-withdrawing effect has a negative impact on the activity profile, where the analogues **6** (4-Cl) and **7** (4-F) showed weak cytotoxicity compared to that of **8** bearing e-releasing functionality (OH).

In regard to positional isomers, the activity's order was **13** (2-CH_3) > **12** (3-CH_3) > **11** (4-CH_3). The high potency is correlated with electron-releasing by +I of CH_3 at p-2 (the preferred position), thus the electron-releasing is a beneficial criteria for cytotoxicity. Conversely, it appeared from the IC_{50}s of compounds **8** (4-OH) and **9** (2-OH) that **8** was slightly more active; this may be attributed to the fact that 4-OH affects the activity *via* both +I and +M effects rather than 2-OH, which shows only +I effects.

Another polar but highly electron-withdrawing compound is compound **10** (4-NO_2), which displayed strong cytotoxicity (IC_{50} 19.41, 11.93 μM), towards HCT116 and MCF-7, respectively. Additionally, moderate activities appeared for compounds **5** (4-H) and **17** (4-COOEt), while both the analogues **15** (4-$COCH_3$) and **16** (4-COOH) bearing strong electron-withdrawing groups are weak cytotoxic agents. Regarding compound **19**, very strong cytotoxicity results (IC_{50} 6.18, 5.11 μM) against HCT116 and

 © 2023 The Author(s). Published by the Royal Society of Chemistry

Open Access Article. Published on 31 October 2023. Downloaded on 10/24/2025 6:18:49 PM.
This article is licensed under a Creative Commons Attribution-NonCommercial 3.0 Unported Licence.

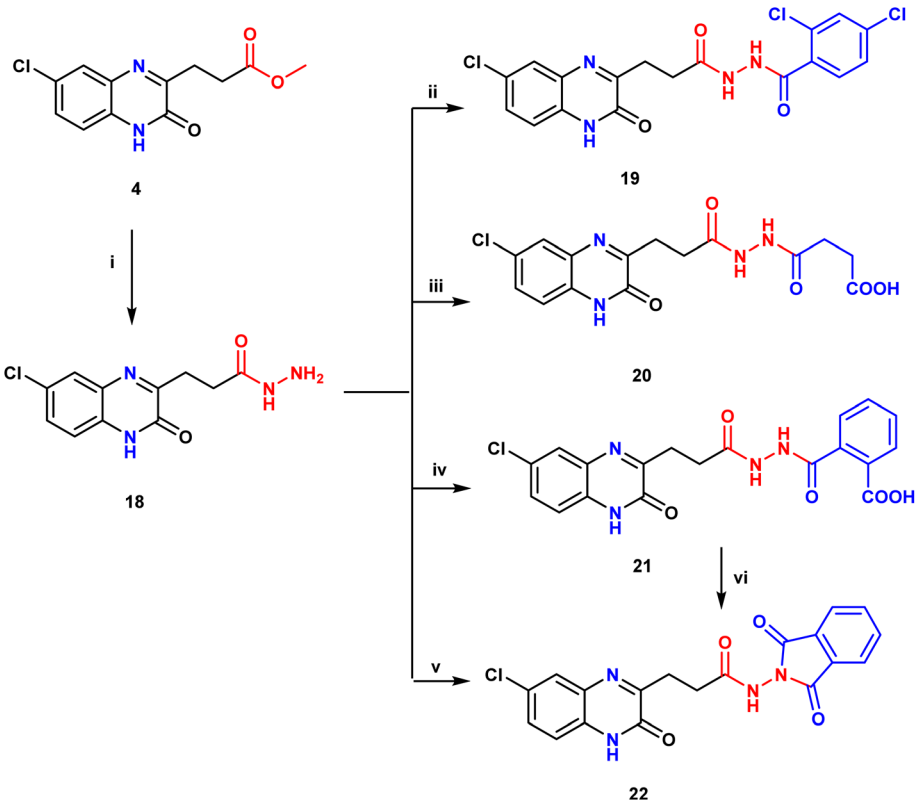

Scheme 2 Reagents and conditions, (i) hydrazine hydrate, EtOH, reflux, 5 h. (ii) 2,4-dichlorobenzoyi chloride, EtOH/DME, reflux, 3 h. (iii) sucdnic anhydride, EtOH/DMF, reflux, 4 h, (iv) phthalic anhydride, EtOH/DME, reflux, 5 h, (v) phthalic anhydride, gl. CH_3COOH, reflux, 4 h, (vi) gl. CH_3COOH, reflux, 2 h.

Table 1 Cytotoxic activity of the new compounds against human tumor cells (IC_{50} μM)[a,b]

Compd. no.	HCT-116	MCF-7	Compd. no.	HCT-116	MCF-7
DOX	9.27 ± 0.3	7.43 ± 0.2	**12**	28.35 ± 2.2	24.56 ± 1.9
Sorafenib	18.60 ± 1.9	16.0 ± 3.6	**13**	22.19 ± 1.9	18.88 ± 1.4
Sunitinib	3.42 ± 0.5	4.77 ± 0.2	**14**	5.81 ± 0.5	4.61 ± 1.1
5	45.52 ± 2.7	39.03 ± 2.4	**15**	84.46 ± 3.9	76.73 ± 3.8
6	62.21 ± 3.3	54.73 ± 3.2	**16**	75.06 ± 3.6	67.23 ± 3.5
7	93.14 ± 4.6	80.39 ± 4.1	**17**	36.02 ± 2.4	31.17 ± 2.2
8	4.72 ± 0.8	3.95 ± 0.2	**19**	6.18 ± 2.1	5.11 ± 0.8
9	7.19 ± 0.7	6.92 ± 0.5	**20**	26.41 ± 3.8	10.17 ± 3.3
10	19.41 ± 1.5	11.93 ± 0.9	**21**	48.17 ± 2.7	41.47 ± 2.5
11	61.35 ± 3.4	53.95 ± 3.1	**22**	37.2 ± 2.3	25.92 ± 1.9

[a] IC_{50} (μM): 1–10 (very strong). 11–20 (strong). 21–50 (moderate). 51–100 (weak) and above 100 (non-cytotoxic). [b] DOX: Doxorubicin.

MCF-7, respectively was noticed. Finally, the cyclized phthalimide derivative **22** exhibited better antitumor activity than the open-chain one, **21** (Table 1).

2.2.2 Cytotoxic evaluation on normal lung fibroblast (WI-38) cell line. The safety profile of the promising compounds **8**, **9**, **14**, **19** and **20** were further investigated *via* the determination of their cytotoxicity's on a human normal cell line (W138) using an MTT assay[33] The results confirmed the higher selectivity indices of these compounds on HCT-116 (SI 3.52–19.97) and on MCF-7 (SI 9.15–23.87) than those of DOX (SI 0.72–0.90) (Table 2).

2.2.3 Mechanistic study

2.2.3.1 In vitro evaluation of VEGFR-2 inhibitory activity (IC_{50}).[37] The most selective cytotoxic derivatives (**8**, **9**, and **14**) exhibiting the greatest SIs were further investigated *in vitro* for their inhibitory activities against VEGFR-2 as a possible mechanism of their antitumor activity. In the meantime, sorafenib was used as a positive control. Half-maximal inhibitory concentration (IC_{50}) values as presented in Table 2 were calculated from the obtained concentration–inhibition response curves. As can be seen from Table 2, the inhibitory effects of VEGFR-2 by our hits (**8**, **9**, and **14**) are ranged from IC_{50}s of

Open Access Article. Published on 31 October 2023. Downloaded on 10/24/2025 6:18:49 PM.
This article is licensed under a Creative Commons Attribution-NonCommercial 3.0 Unported Licence.

Table 2 Cytotoxicity on WI-38, selectivity indices and VEGFR-2 inhibitory activity (IC_{50} μM)

Compd no.	WI-38	HCT-116	SI	MCE-7	SI	VEGFR-2
8	94.27 ± 3.5	4.72 ± 0.8	19.97	3.95 ± 0.2	23.87	0.109
9	86.11 ± 4.1	7.19 ± 0.7	11.98	6.92 ± 0.5	12.44	0.131
14	88.72 ± 3.9	5.81 ± 0.5	15.27	4.61 ± 1.1	19.25	0.076
19	71.60 ± 2.8	6.18 ± 2.1	11.58	5.11 ± 0.8	14.01	—
20	93.04 ± 2.2	26.41 ± 3.8	3.52	10.17 ± 3.3	9.15	—
DOX	6.72 ± 0.5	9.27 ± 0.3	0.72	7.43 ± 0.2	0.90	—
Sunitinib	—	3.42 ± 0.5	—	4.77 ± 0.2	—	0.139 (ref. 35)
Sorafenib	—	18.60 ± 1.9	—	16.0 ± 3.6	—	0.076

0.076–0.131 μM. It became evident that compound **14** had the highest VEGFR-2 inhibitor potency (IC_{50} 0.076 μM), making it equivalent to the reference standard sorafenib. It was interesting to see that it had 1.83 times the potency of sunitinib (IC_{50} 0.139 μM) (Table 2 and Fig. 2).

2.2.3.2 Quantitative determination of VEGFR-2 in MCF-7 cell line:.[38] According to research, VEGF/VEGFR-2 activation is essential for the angiogenesis process and has been identified as a key factor in tumor vascularization.[39] So, we measured the VEGFR-2 concentrations in MCF-7 cell line. Our findings showed that compound **14** reduces VEGFR-2 production in medium from MCF-7 cells (170.2 4 pg ml^{-1}) in comparison to untreated cells (330.8 4.1 pg ml^{-1}) (Fig. 3). These outcomes support the therapeutic targeting of compound **14** as a VEGFR2 inhibitor.

*2.2.3.3 Effect of compound **14** on angiogenesis (VEFG-A) level.*[40] It is known that angiogenesis plays a crucial role in the progression and advancement of tumors in different cancer types, including breast cancer. Among pro-angiogenic factors, vascular endothelial growth factor (VEGF-A) is a prominent target that encourages tumor growth and metastasis. Therefore, we also evaluated the concentration of VEGF in culture media of MCF-7 after treatment with **14** (Fig. 4). ELISA analysis showed that **14** suppressed VEGF-A secretion in media of MCF-7 when compared to the control group. These findings suggested that **14** could be valuable *in vivo* tumor suppression *via* inhibition of angiogenesis.

2.2.4 Cell cycle analysis.[41] Cell cycle analysis data, as shown in Fig. 5a–c clearly showed that the target compound **14** significantly increased the proportion of cells in the Pre-G1 phase compared to control by about 1.38 folds and the percentage of cells in the G2/M phase by 3.59 folds in relation to the control. The fraction of cells in the Go/G1 and S stages of the cell cycle decreased along with this striking increase. According to the Pre-G1 and G2/M phase data, compound **14** promotes apoptosis at the Pre-G1 phase and stops the cell cycle at the G2/M phase.

2.2.5 Annexin V-FITC apoptosis assay. By using a flow cytometer, experiments on the binding of Annexin V were conducted to verify the induction of apoptosis by compound **14**.[42]

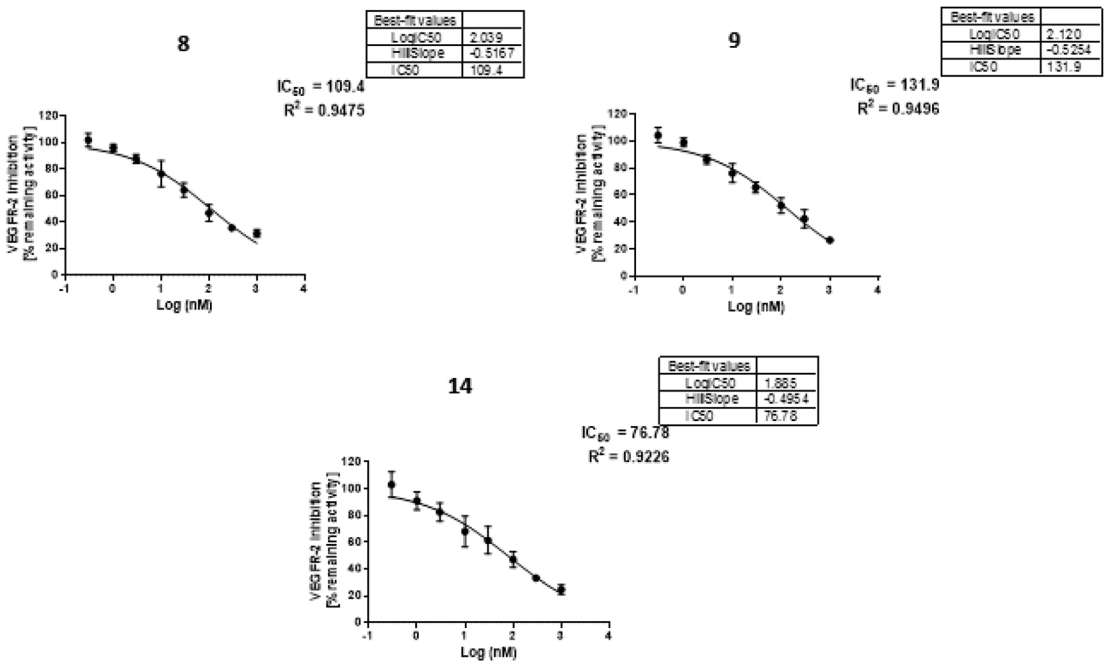

Fig. 2 The inhibitory effect of quinoxaline derivatives **8**, **9** and **14** against VEGFR-2.

 © 2023 The Author(s). Published by the Royal Society of Chemistry

Open Access Article. Published on 31 October 2023. Downloaded on 10/24/2025 6:18:49 PM.
This article is licensed under a Creative Commons Attribution-NonCommercial 3.0 Unported Licence.

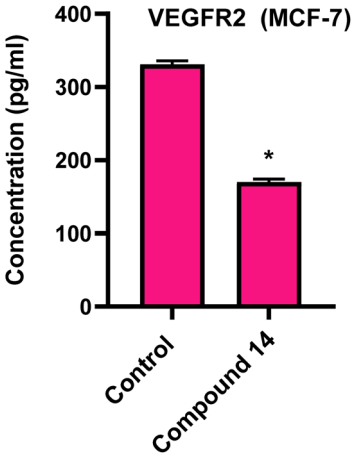

Fig. 3 Secretion of VEGFR2 in cell culture media of MCF-7 cells treated with IC50 of compound **14** for 24 h, was measured by ELISA kits. Results were expressed as means ± SD of samples performed in triplicates.

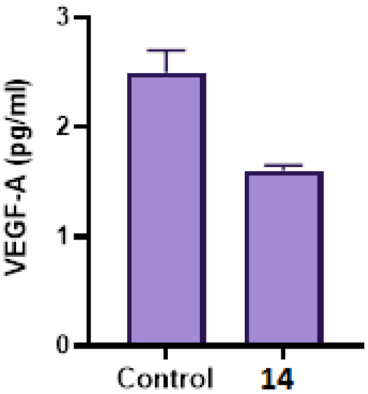

Fig. 4 VEGF-A concentrations in cell culture media of MCF-7 breast cancer cell line using ELISA assay following treatment with **14**. Results were expressed as means ± SD of samples performed in triplicates.

In comparison to the control experiment, the administration of compound **14** to MCF-7 cells increased the early apoptosis ratio (lower right quadrant of the cytogram) from 0.15 to 2.05 and the late apoptosis ratio (upper right quadrant of the cytogram) from 0.73 to 6.25. The target chemical **14**, displayed high apoptotic effect and was 10.15 times more potent than the control experiment, as shown from a comparative investigation of total apoptosis. The results imply that **14** induced apoptosis through the programmed cell death and necrotic pathways (Table 3, Fig. 6a and b).

The quadrants in the cytograms represent the following: Necrotic cells (higher left quadrant of the cytogram); late apoptotic cells (higher right quadrant of the cytogram); non-apoptotic and non-necrotic cells (living cells) (lower left quadrant of the cytogram); early apoptotic cells (lower right quadrant of the cytogram).

2.2.6 Effect of compound 14 on active caspase-3. Apoptosis is characterized by activation of the caspase-3 pathway, which can be utilized in cellular assays to measure the activators and inhibitors of the "death cascade".[43] The impact on caspase-3 of the most potent quinoxaline derivative (**14**) was assessed. According to the results, **14** increased the level of caspase-3 by roughly 8.84 and 1.1 folds in comparison to the control and sunitinib, respectively. Accordingly, the data showed that the quinoxaline derivative **14** has the ability to induce apoptosis (Table 4 and Fig. 7a).

2.2.7 Effect on active p53 level.[44] The tumor suppressor gene p53, which has undergone mutation in more than 50% of human malignancies, is the chief gatekeeper of the genome. Its action prevents the growth of tumors. The p53 gene, which functions as a transcriptional regulator and influences many biological processes, including apoptosis and growth arrest, produces the p53 protein. It is thought that p53's ability to control the expression of a variety of target promoters, including p21, Bax, bcl-2, CDK2, and PUMA, may be the reason for its capacity to cause apoptosis and growth arrest. Data collected showed that **14** substantially raised the expression of p53 on MCF-7 cells by around 15.59 folds (fld) in comparison to the control and 1.24 folds in comparison to sunitinib. Thus, it strongly shifted MCF-7 cancer cells towards apoptosis (Table 4 and Fig. 7b).

2.2.8 Effect on mitochondrial apoptosis pathway proteins BAX and BCL2. The apoptotic process in mitochondria is regulated by the BCL2 protein family. These include the proteins BCL2 and BAX,[45] which precisely regulate this planned process since BCL2 inhibits apoptosis (is antiapoptotic) and BAX speeds it up (is proapoptotic). As a result, the precise balance between these two unique proteins serves as a measure of a cell's capacity to undergo apoptosis.[46] A variety of direct BAX activators have been shown to have promise for cancer therapy due to the advantages of specificity and the potential to overcome chemo- and radio-resistance. The level of the proapoptotic protein BAX was significantly increased (4.3 fold change) by the most effective quinoxaline-3-propanamide **14**, while the level of the antiapoptotic protein Bcl-2 was significantly decreased by it (0.448 fold change) compared to the control and the reference drug staurosporine (Bax 7.55 and BCL2 0.33 fold change) *c.f.* Table 4 and Fig. 7c.

2.3. Molecular modeling study

2.3.1 *In silico* evaluation of physicochemical and ADME properties. For the anticipated biologic events to take place, a powerful molecule needs to reach its target in the body in sufficient concentration and remain there for an adequate amount of time in a bioactive form. It is understood that a drug's ideal qualities should contain both adequate pharmacokinetic features and its efficacy. A drug's toxicity depends on its absorption, distribution, metabolism, and excretion (ADME) parameters in addition to its inherent pharmacological characteristics. High drug attrition rates in the last stages of drug development have been associated with poor ADME features, such as the generation of hazardous metabolites.

Here, using the online version of SwissADME, a computational assessment of the synthesized compounds was carried

Open Access Article. Published on 31 October 2023. Downloaded on 10/24/2025 6:18:49 PM.
This article is licensed under a Creative Commons Attribution-NonCommercial 3.0 Unported Licence.

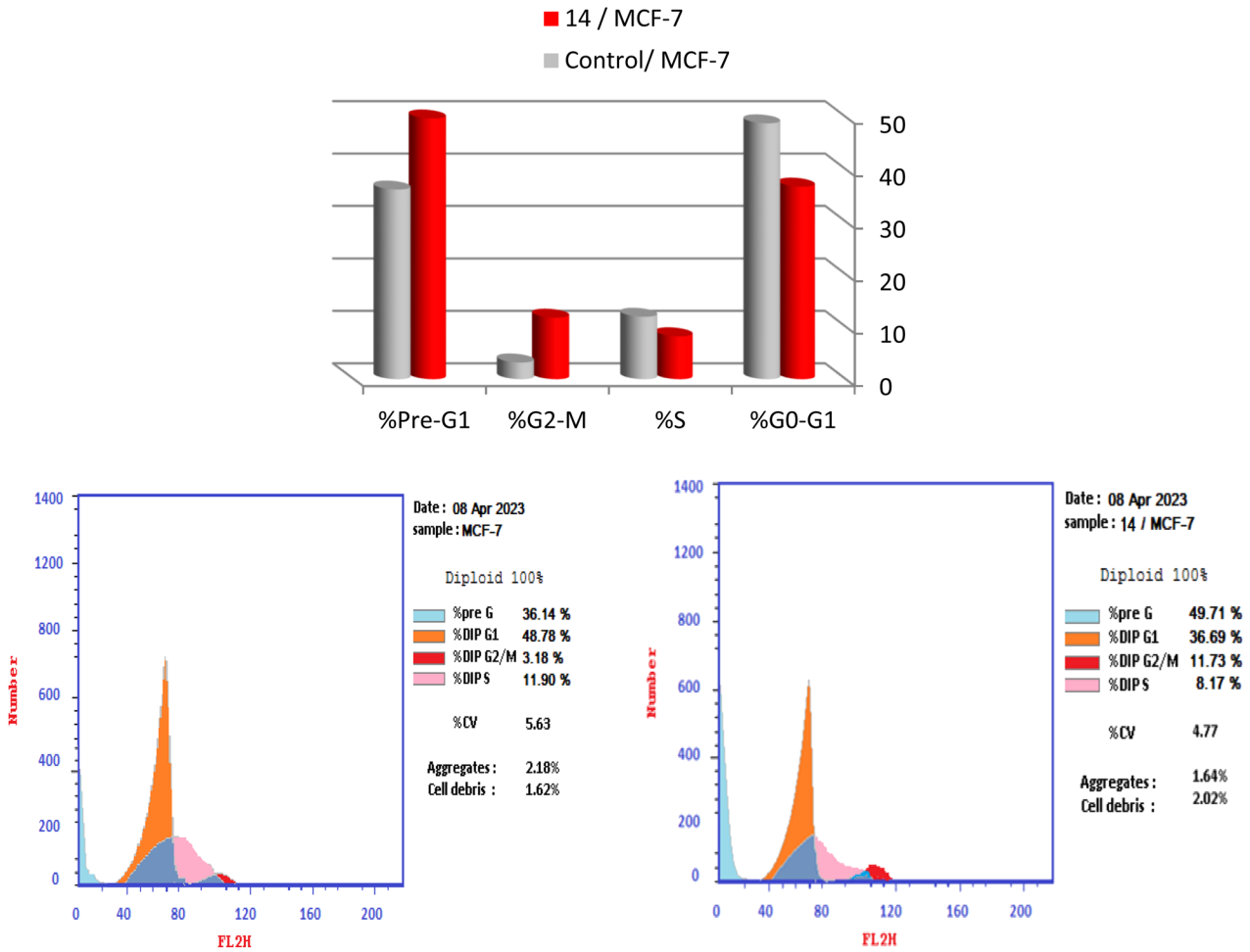

Fig. 5 (a) Cell cycle analysis of control and compound 14 in MCF-7 cell line. (b) Cell cycle analysis of MCF-7 cells treated with DMSO, (c) cell cycle analysis of MCF-7 cells treated with compound **14**.

Table 3 Effect of compound **14** on apoptosis of MCF-7 cells

Sample	Total	Early apoptosis	Late apoptosis	Necrosis
14/MCF-7	22.03	2.05	6.25	12.73
Control/MCF-7	2.17	0.15	0.73	1.29

out to assess the physicochemical and ADME properties.[47] Regarding Lipinski's rule for oral medications, which indicates that a molecule is more likely to be absorbed or permeated if its molecular weight is less than 500 g mol^{-1}, its $M \log P$ value is lower than 5, and it has at least 5 H-donor and 10 H-acceptor atoms.[48] While Veber's rule[49] specifies polar surface area (PSA) 140 and rotatable bond count 10 as drug-likeness restrictions, respectively.[50] It was discovered that all of the synthesized compounds have Lipinski zero violations in their physicochemical parameters and every chemical has rotatable bonds between 5 and 8 that indicate molecular flexibility for its bio

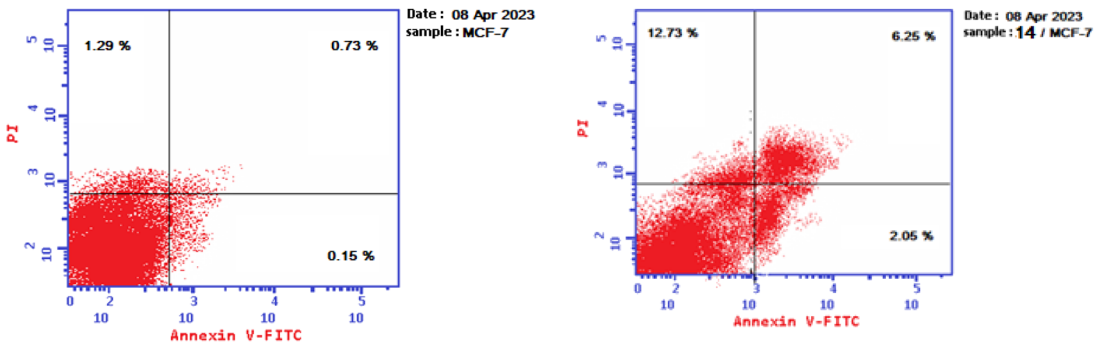

Fig. 6 (a) Effect of control on apoptosis of MCF-7 cells. (b) Effect of 14 on apoptosis of MCF-7 cells.

 © 2023 The Author(s). Published by the Royal Society of Chemistry

Open Access Article. Published on 31 October 2023. Downloaded on 10/24/2025 6:18:49 PM.
This article is licensed under a Creative Commons Attribution-NonCommercial 3.0 Unported Licence.

Table 4 The effect of compound **14** on the level of caspase-3, p53, BAX and BCL2

Sample	Caspase 3 (pg ml^{-1})	Fld	p53 (pg ml^{-1})	Fld	BAX fold change	BCL2 fold change
14	423.10 ± 11.24	8.836	345.83 ± 7.44	15.585	4.336	0.448
Sunitinib	384.53 ± 8.40	8.031	278.34 ± 5.27	12.543	—	—
Staurosporine	—	—	—	—	7.5517	0.3248
Control	47.88 ± 13.15	1	22.19 ± 8.39	1	1	1

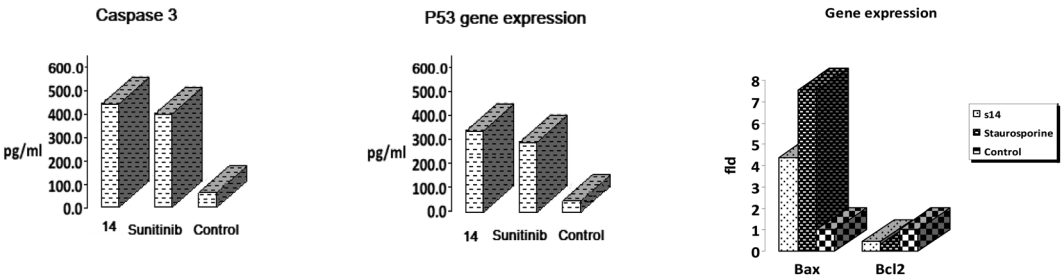

Fig. 7 The effect of **14** on (a), caspase-3. (b) p53, (c) BAX and BCL2.

Table 5 Physicochemical properties based on Lipinski's rule of five and number of rotatable bonds

Cpd. no.	HBD	HBA	$M \log P$	MWt	No. of Rot. bonds	Lipinski's violations	Veber's violations
5	2	3	2.39	327.76	5	0	0
6	2	3	2.89	362.21	5	0	0
7	2	4	2.78	345.76	5	0	0
8	3	4	1.85	343.76	5	0	0
9	3	4	1.85	343.76	5	0	0
10	2	5	1.40	372.76	6	0	0
11	2	3	2.63	341.79	5	0	0
12	2	3	2.63	341.79	5	0	0
13	2	3	2.63	341.79	5	0	0
14	2	4	2.08	357.79	6	0	0
15	2	4	1.97	369.80	6	0	0
16	3	5	2.02	371.77	6	0	0
17	2	5	2.47	399.83	8	0	0
19	3	4	3.15	439.68	7	0	0
20	4	6	0.57	366.76	9	0	1
21	4	6	1.83	414.80	8	0	1
22	2	5	1.93	396.78	5	0	0
Sorafenib	3	7	2.91	464.82	9	0	0
Sunitinib	3	4	2.06	398.47	8	0	0

target (Table 5). In addition, all hits pass muster under the Veber guidelines used for screening.

The topological polar surface area (TPSA) is known to be a reliable indication of drug penetration through the blood–brain barrier (TPSA less than 60 Å^2) and intestinal drug absorption (TPSA less than 140 Å^2). All compounds exhibit computational TPSA values in the appropriate range for permeating cell membranes so they obey Veber's rule except compounds **20** and **21** (TPSA 141 Å^2). Moreover, absorption (% ABS) was calculated using the formula% ABS = 109 − (0.345 × TPSA), and it was discovered that the calculated % ABS of all these hits ranged between 60.26% and 83.17%, indicating that these synthetic derivatives may have the necessary cell membrane permeability and bioavailability (Table 6).

The synthesized compounds' pharmacokinetic and medicinal chemistry parameters (Table 7) made it clear that all of the derivatives had high gastrointestinal absorption and that the majority of them did not cross the blood–brain barrier, guaranteeing that these systemically targeted molecules would have few to no CNS side effects. Analyzing the P-glycoprotein (P-gp) non-substrate candidature during preclinical analysis trials was another crucial factor. P-gp performs the function of an efflux transporter, expelling medicines, other substances, and its substrate from the cell. This sounds like an explanation for why anticancer chemotherapeutic drugs like Imatinib, Lonafarnib, and Taxanes are ineffective. The fact that not all hits are P-gp protein substrates (Table 7) suggests that these hits have

Open Access Article. Published on 31 October 2023. Downloaded on 10/24/2025 6:18:49 PM.
This article is licensed under a Creative Commons Attribution-NonCommercial 3.0 Unported Licence.

Table 6 The topological polar surface area (TPSA), and ABS%

Comp. no.	TPSA	ABS%
5	74.85	83.17
6	74.85	83.17
7	74.85	83.17
8	95.08	76.19
9	95.08	76.19
10	120.67	67.36
11	74.85	83.17
12	74.85	83.17
13	74.85	83.17
14	84.08	79.99
15	91.92	77.28
16	112.15	70.30
17	101.15	74.10
19	103.95	73.13
20	141.25	60.26
21	141.25	60.26
22	112.23	70.28
Sorafenib	92.35	77.13
Sunitinib	77.23	108.92

a reduced likelihood of effluxing out of the cell and committing maximal effect.

The amount of drug present in the plasma is measured by bioavailability, which is regarded as the most important factor influencing absorption. It's interesting to note that all of the synthetic compounds have high bioavailability ratings on par with sorafenib and sunitinib.

Chemical substances known as pan-assay interference chemicals (PAINS) frequently produce false-positive findings in high-throughput screening. Instead of directly affecting one intended target, PAINS typically respond non-specifically with many biological targets. Checking any PAINS alert of the recently created derivatives is crucial. SwissADME did a PAIN that showed no alarms for any of the hits. The SwissADME Synthetic Accessibility (SA) Score is based mainly on the supposition that the frequency of molecular fragments in 'really' attainable molecules correlates with the ease of synthesis; the score is normalized to range from 1 (very easy) to 10 (very difficult). SA scores of all the analogues were found to be between 2.57 and 2.85, indicating that they can be easily synthesized on a large scale.

The *in silico* ADME prediction analysis results showed that the synthesized compounds exhibit the computational assessment and are therefore viewed as a pharmacologically active framework that should be taken into consideration when moving forward with potential hits.

2.3.2 Molecular docking study. Type I and Type II VEGFR-2 inhibitors can be distinguished based on their binding profiles. Type I inhibitors connect with the ATP binding site and have low selectivity, but type II inhibitors have great selectivity and bind to both the ATP site and the allosteric hydrophobic site. The front and rear pockets make up the VEGFR-2 active site's straightforward structure. Glu917 and Cys919 are two crucial residues connected to the ATP-binding front pocket. Glu885 and Asp1046 are located in the rear hydrophobic pocket.[51] Inhibitors of VEGFR-2 interact with the receptor's ATP-binding site in the catalytic domain to stop the processes of dimerization and autophosphorylation. This finally stops the signaling cascade from starting, reduces cell vascular permeability, and inhibits angiogenesis.

Using MOE 2014 software, it is possible to investigate the binding interaction of the target compounds using the known crystal structure of VEGFR-2 (PDB ID: 4ASD).[52] Reference molecules were the co-crystallized ligands sorafenib and sunitinib. The results of the docking studies demonstrated that our hit **14** had a high affinity for VEGFR-2 in comparison to the reference molecules. Sorafenib, a co-crystallized ligand, was re-

Table 7 Pharmacokinetic properties and medicinal chemistry parameters

Compd no.	GI absorption	BBB permeation	P-gp substrate	Bioavailability score	PAINS alerts	Synthetic accessibility
5	High	Yes	No	0.55	0	2.58
6	High	Yes	No	0.55	0	2.60
7	High	Yes	No	0.55	0	2.59
8	High	No	No	0.55	0	2.57
9	High	No	No	0.55	0	2.61
10	High	No	No	0.55	0	2.68
11	High	Yes	No	0.55	0	2.63
12	High	Yes	No	0.55	0	2.65
13	High	Yes	No	0.55	0	2.66
14	High	No	No	0.55	0	2.66
15	High	No	No	0.55	0	2.69
16	High	No	No	0.56	0	2.60
17	High	No	No	0.55	0	2.85
19	High	No	No	0.55	0	2.96
20	High	No	Yes	0.56	0	2.91
21	High	No	Yes	0.56	0	2.98
22	High	No	No	0.55	0	2.83
Sorafenib	Low	No	No	0.55	0	2.87
Sunitinib	High	Yes	Yes	0.55	0	3.58

 © 2023 The Author(s). Published by the Royal Society of Chemistry

Open Access Article. Published on 31 October 2023. Downloaded on 10/24/2025 6:18:49 PM.
This article is licensed under a Creative Commons Attribution-NonCommercial 3.0 Unported Licence.

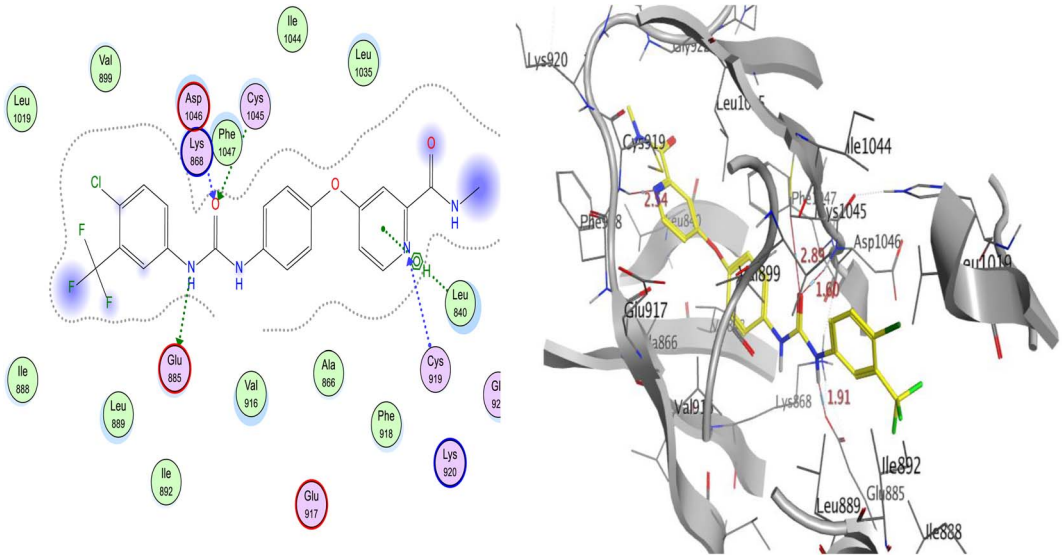

Fig. 8 The proposed 2D (left) and 3D (right) binding interaction of co-crystalized sorafenib with 4ASD.

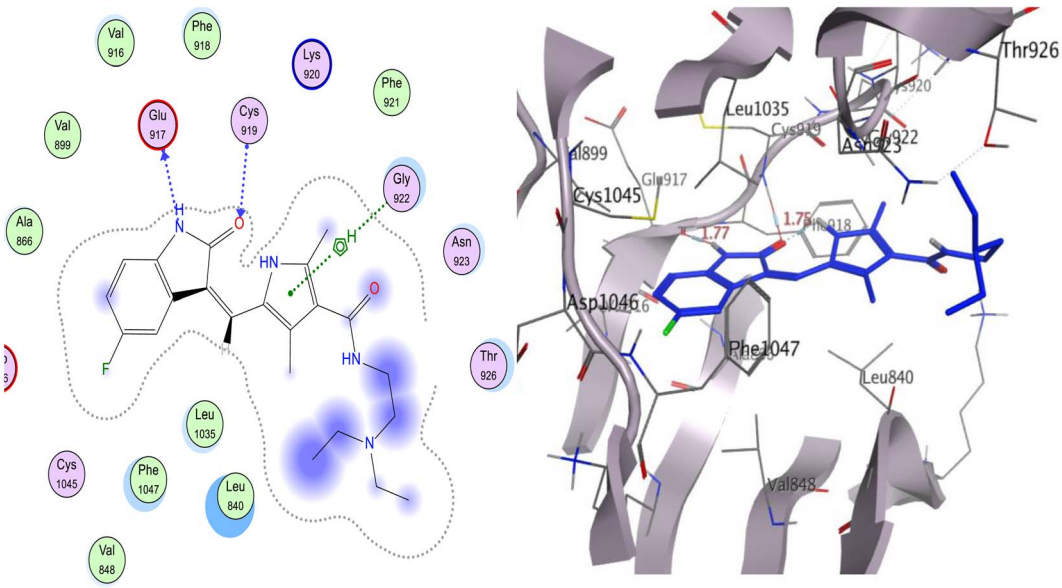

Fig. 9 The proposed 2D (left) and 3D (right) binding interaction of the parent sunitinib with 4ASD.

docked against VEGFR-2 to verify the docking techniques. The applied docking methodology was validated by the resulting RMSD of 0.88 (Fig. 8).

Sorafenib's docking score was −10.74 kcal mol^{-1}, and the urea moiety's three hydrogen bonds with the critical amino acids Glu885, Asp1046, and Cys1045 allowed it to bind to the receptor. The hinge region, where the pyridine moiety established a hydrogen link with Cys919 and an arene–H bond with Leu840, was also occupied by the *N*-methylpicolinamide moiety. Additionally, Leu840, Val916, Leu889, Phe1047, and Leu1035 all showed five hydrophobic contacts (Fig. 8).

Sunitinib inhibits the ATP pocket by an H-bond acceptor/donor interaction between two HB of the indolin-2-one core and Cys919 and Glu917 in the hinge region, together with the pyrrole group as a linker connected to Gly922 *via* arene-H. Docking experiments showed that sunitinib had a binding energy of −5.76 kcal mol^{-1}. Leu840, Phe1047, Leu1035, Gly922, Val916, and Phe918 were among the hydrophobic interactions that the sunitinib tail was involved in (Fig. 9).

Our hit **14** had an incredibly low free binding energy of −11.58 kcal mol^{-1} when compared to sorafenib and sunitinib. It showed 2HBA between the quinox-CO, Phe918, and Cys919 in the hinge region. Quinox-NH was also shared by 1HBD with Glu917. On the other hand, 1HBD also provided CH_2 of the linker to the critical amino acid Cys919. Unexpectedly, the gate area's Asp1046 bound to the chloro functionality by HBD,

Open Access Article. Published on 31 October 2023. Downloaded on 10/24/2025 6:18:49 PM.
This article is licensed under a Creative Commons Attribution-NonCommercial 3.0 Unported Licence.

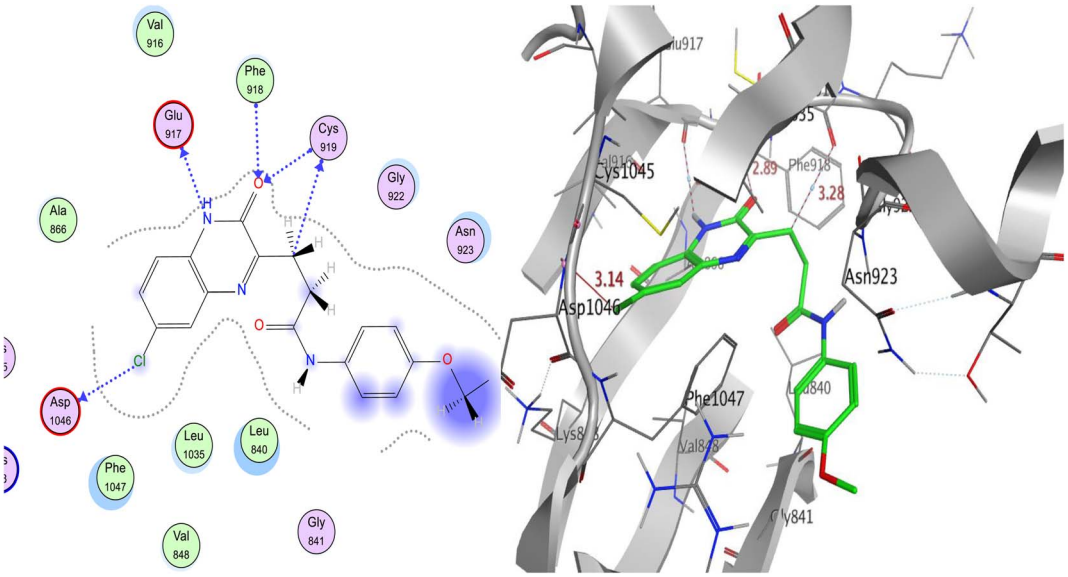

Fig. 10 The proposed 2D (left) and 3D (right) binding interaction of compound **14**.

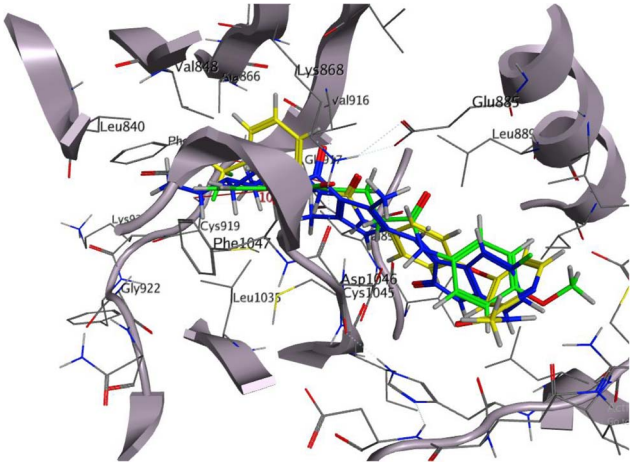

Fig. 11 Overlay docking alignment of sorafenib (yellow), sunitinib (blue), and **14** (green) in the active site of VEGFR-2.

therefore it is supposed that **14** may act as type II inhibitor of VEGFR-2. Additionally, several hydrophobic interactions involving the methoxyl group, terminal phenyl, and aliphatic linker helped the compound attach to VEGFR-2 (Fig. 10). These interactions included Gly922, Asn923, Val916, Phe1047, Le840, and Leu1035. Overlay docking alignment was also carried out between sorafenib (yellow), sunitinib (blue), and **14** (green) in the active site of VEGFR-2 to verify the target chemical **14**'s mode of action as a VEGFR-2 inhibitor (Fig. 11).

3. Conclusion

Thirteen novel quinoxaline-3-propamide derivatives were created using various substitutions, and their SARs as potential anticancer agents that target the VEGFR-2 enzyme were examined. Eight substances had cytotoxic effects on HCT-116 and MCF-7 that ranged from extremely strong to mild. The top three substances (**8**, **9** and **14**) were then further examined as potential VEGFR-2 inhibitors. Intriguingly, **14** was equivalent to sorafenib (IC_{50} 0.076 M) and 1.83 folds more potent (IC_{50} 0.076 M) than the reference medication, sunitinib (IC_{50} 0.139 M). It reduces VEGFR-2 production in MCF-7 cells when compared to untreated cells. What's more, it lowers VEGF-A level more than control in MCF-7 cells which suggested that **14** could be valuable *in vivo* tumor suppression *via* inhibition of angiogenesis. Cell cycle analysis was used to conduct a more detailed assessment of the most active compound, **14**, utilizing the MCF-7 cell line. In comparison to the control, it markedly boosted the pre-G phase while halting the G2/M phase of the cell cycle. Additionally, a flow cytometry assay utilizing Annexin V was performed on it, and the outcomes demonstrated an increase in the overall apoptosis percentage compared to the control. Once more, it increased the expression of caspase-3, p53, and BAX; while reduced the BCL2 level than the control experiment; both of which are apoptosis inducers. Docking studies supported our proposed mode of action for **14** as a VEGFR-2 inhibitor and demonstrated nearly identical binding characteristics to the co-crystallized inhibitor (TSA). Because it is not a P-gp substrate and does not permeate the BBB, our hit **14** had more favorable pharmacokinetic characteristics than sunitinib.

4. Experimental section

4.1. Chemistry

Reagents and solvents were ordered from regular commercial suppliers and used without further purification. The reported yields apply to distilled products. All reactions were routinely checked with thin-layer chromatography (TLC) of Merck Silica Gel 60 F254 (0.25 mm thick) and visualization with a UV lamp. The melting points were measured in open capillary tubes using the Stuart SMP3 apparatus. IR spectra (KBr) were measured on

 © 2023 The Author(s). Published by the Royal Society of Chemistry

Open Access Article. Published on 31 October 2023. Downloaded on 10/24/2025 6:18:49 PM.
This article is licensed under a Creative Commons Attribution-NonCommercial 3.0 Unported Licence.

a Shimadzu FT/IR 1650 (PerkinElmer) spectrometer. ^{1}H and ^{13}C NMR spectra were recorded on a Brüker Advance-400 instrument (400 MHz for ^{1}H and 100 MHz for ^{13}C) in DMSO-d_6 Chemical shifts (δ) are reported in ppm relative to TMS as an internal standard, or to the solvent in which the spectrum was recorded. Mass spectra were performed on a Shimadzu GS/MS-QP 2010 plus spectrometer at 70 eV.

4.2 General procedure

Equimolar amounts of ethyl propanoate ester **4** and different substituted anilines were refluxed in ethanol/DMF (15/5) for 8–16 h. The reaction medium was cooled and poured into ice water. The precipitate was filtered, dried and crystalized from ethanol to afford the corresponding anilides **5–17**.

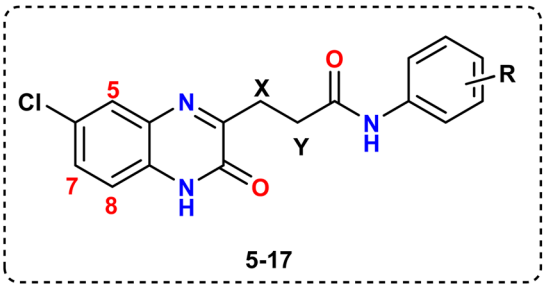

4.2.1 3-(6-Chloro-1,2-dihydro-2-oxoquinoxalin-3-yl)-*N*-phenylpropanamide (5). Dark brown powder; yield (68%); mp. 94–96 °C; IR (KBr, cm^{-1}): 3271, 3222 (2NH), 1693, 1658 (2C=O); ^{1}H NMR (400 MHz, DMSO-d_6) δ (ppm): 1.68 (t, 2H, CH_2x, J = 7.6 Hz), 2.34 (t, 2H, CH_2y, J = 7.6 Hz), 6.87 (t, 1H, Ar–H_4), 7.07 (t, 2H, Ar–$H_{3,5}$, J = 8 Hz), 7.41 (d, 2H, Ar–$H_{2,6}$, J = 8 Hz), 7.60 (d, 1H, quinoxaline-H_7, J = 8 Hz), 8.23 (s, 1H, quinoxaline-H_5), 8.33 (d, 1H, quinoxaline-H_8, J = 8 Hz), 10.31, 12.59 (2s, 2NH, D_2O exchangeable). ^{13}C NMR (DMSO-d_6) δ (ppm): 29.34 (CH_2), 31.50 (CH_2), 119.12, 120.34, 120.50, 120.57, 125.45, 125.75, 126.12, 126.19, 126.45, 128.34, 129.50, 130.57, 131.12 (13 Ar–C), 167.12, 170.34 (2C=O). MS m/z: 327.12 (21.53%, M$^+$), 329.14 (7.16%, M^{+2}), 76.09 (100). Anal. calcd for: $C_{17}H_{14}ClN_3O_2$ (327.76): C, 62.30; H, 4.31; N, 12.82%, found: C, 62.73; H, 4.67; N, 12.40%.

4.2.2 3-(6-Chloro-1,2-dihydro-2-oxoquinoxalin-3-yl)-*N*-(4-chlorophenyl) propanamide (6). Black powder; yield (79%); mp. 180–182 °C; IR (KBr, cm^{-1}): 3394, 3225 (2NH), 1692, 1670 (2C=O); ^{1}H NMR (400 MHz, DMSO-d_6) δ (ppm): 1.66 (t, 2H, CH_2x, J = 8 Hz), 2.33 (t, 2H, CH_2y, J = 8 Hz), 7.14 (d, 1H, quinoxaline-H_7, J = 7.6 Hz), 7.64 (d, 2H, Ar–$H_{3,5}$, J = 8 Hz), 7.83 (d, 2H, Ar–$H_{2,6}$, J = 8 Hz), 7.96 (s, 1H, quinoxaline-H_5), 8.02 (d, 1H, quinoxaline-H_8, J = 7.6 Hz), 11.51, 11.64 (2s, 2NH, D_2O exchangeable). ^{13}C NMR (DMSO-d_6) δ (ppm): 29.03 (CH_2), 30.81 (CH_2), 121.68, 128.62, 128.69, 129.29, 129.34, 134.35, 134.36, 135.62, 136.28, 137.69, 145.29, 147.27, 148.21 (13 Ar–C), 164.09, 165.69 (2C=O). MS m/z: 361.53 (62.18%, M$^+$), 363.20 (20.46%, M^{+2}), 365.14 (8.06%, M^{+4}), 74.03 (100). Anal. calcd for: $C_{17}H_{13}Cl_2N_3O_2$ (362.21): C, 56.37; H, 3.62; N, 11.60%, found: C, 56.81; H, 3.93; N, 11.15%.

4.2.3 3-(6-Chloro-1,2-dihydro-2-oxoquinoxalin-3-yl)-*N*-(4-fluorophenyl) propanamide (7). Pale brown powder; yield (82%); mp. 128–130 °C; IR (KBr, cm^{-1}): 3448, 3371 (2NH), 1685, 1623 (2C=O); ^{1}H NMR (400 MHz, DMSO-d_6) δ (ppm): 1.72 (t, 2H, CH_2x, J = 8 Hz), 2.32 (t, 2H, CH_2y, J = 8 Hz), 6.85 (d, 1H, quinoxaline-H_7, J = 8.4 Hz), 6.99 (d, 2H, Ar–$H_{2,6}$, J = 8 Hz), 7.40 (t, 2H, Ar–$H_{3,5}$, J = 8 Hz), 7.60 (s, 1H, quinoxaline-H_5), 7.80 (d, 1H, quinoxaline-H_8, J = 8.4 Hz), 11.17, 11.32 (2 s, 2NH, D_2O exchangeable). ^{13}C NMR (DMSO-d_6) δ (ppm): 29.46 (CH_2), 31.28 (CH_2), 151.57, 115.68, 116.70, 116.78, 118.78, 121.02, 121.78, 122.02, 122.25, 123.27, 131.18, 136.21, 143.32 (13 Ar–C), 166.10, 170.13 (2C=O). MS m/z: 345.04 (18.43%, M$^+$), 347.11 (5.96%, M^{+2}), 77.14 (100). Anal. calcd for: $C_{17}H_{13}ClFN_3O_2$ (345.46): C, 59.05; H, 3.79; N, 12.15%, found: C, 59.55; H, 3.23; N, 12.62%.

4.2.4 3-(6-Chloro-1,2-dihydro-2-oxoquinoxalin-3-yl)-*N*-(4-hydroxyphenyl) propanamide (8). Brown powder; yield (74%); mp. 140–142 °C; IR (KBr, cm^{-1}): 3410 (OH), 3324, 3249 (2NH), 1693, 1624 (2C=O); ^{1}H NMR (400 MHz, DMSO-d_6) δ (ppm): 1.69 (t, 2H, CH_2x, J = 7.2 Hz), 2.34 (t, 2H, CH_2y, J = 7.2 Hz), 6.74 (d, 2H, Ar–$H_{3,5}$, J = 8 Hz), 7.00 (d, 1H, quinoxaline-H_7, J = 7.6 Hz), 7.37 (s, 1H, quinoxaline-H_5), 7.50 (d, 2H, Ar–$H_{2,6}$, J = 8 Hz), 7.78 (d, 1H, quinoxaline-H_8, J = 7.6 Hz), 9.83, 12.37 and 12.48 (3s, OH, 2NH, D_2O exchangeable). ^{13}C NMR (DMSO-d_6) δ (ppm): 29.87 (CH_2), 30.69 (CH_2), 126.52, 127.33, 128.42, 129.87, 130.34, 132.37, 133.50, 134.24, 137.28, 137.29, 137.30, 140.71, 150.37 (13 Ar–C), 164.32, 168.33 (2C=O). MS m/z: 343.19 (27.20%, M$^+$), 345.09 (9.56%, M^{+2}), 71.93 (100). Anal. calcd for: $C_{17}H_{14}ClN_3O_3$ (343.76): C, 59.40; H, 4.10; N, 12.22%, found: C, 59.82; H, 4.43; N, 12.63%.

4.2.5 3-(6-Chloro-1,2-dihydro-2-oxoquinoxalin-3-yl)-*N*-(2-hydroxy phenyl)propanamide (9). Brown powder; yield (81%); mp. 235–237 °C; IR (KBr, cm^{-1}): 3455 (OH), 3322, 3227 (2NH), 1684, 1622 (2C=O); ^{1}H NMR (400 MHz, DMSO-d_6) δ (ppm): 1.66 (t, 2H, CH_2x, J = 7.6 Hz), 2.35 (t, 2H, CH_2y, J = 7.6 Hz), 6.93 (t, 1H, Ar–H_5, J = 8 Hz), 7.05 (d, 1H, Ar–H_3, J = 8 Hz), 7.14 (t, 1H, Ar–H_4, J = 8 Hz), 7.43 (d, 1H, quinoxaline-H_7, J = 8 Hz), 7.63 (s, 1H, quinoxaline-H_5), 7.64 (d, 1H, Ar–H_6, J = 8 Hz), 7.83 (d, 1H, quinoxaline-H_8, J = 8 Hz), 9.85, 11.09 and 11.12 (3 s, OH, 2NH D_2O exchangeable). ^{13}C NMR (DMSO-d_6) δ (ppm): 29.48 (CH_2), 30.32 (CH_2), 120.12, 126.32, 128.20, 129.40, 130.47, 134.60, 134.77, 135.47, 135.60, 135.78, 137.37, 137.38, 138.90 (13 Ar–C), 165.47, 170.50 (2C=O). MS m/z: 343.23 (31.89%, M$^+$), 345.14 (10.03%, M^{+2}), 89.1 (100). Anal. calcd for: $C_{17}H_{14}ClN_3O_3$ (343.76): C, 59.40; H, 4.10; N, 12.22%, found: C, 59.67; H, 4.38; N, 12.42%.

4.2.6 3-(6-Chloro-1,2-dihydro-2-oxoquinoxalin-3-yl)-*N*-(4-nitrophenyl) propanamide (10). Shiny black powder; yield (63%); mp. 238–240 °C; IR (KBr, cm^{-1}): 3367, 3166 (2NH), 1693, 1654 (2C=O), 1508, 1369 (NO_2); ^{1}H NMR (400 MHz, DMSO-d_6) δ (ppm): 1.75 (t, 2H, CH_2x, J = 6.4 Hz), 2.35 (t, 2H, CH_2y, J = 6.4 Hz), 7.39 (d, 1H, quinoxaline-H_7, J = 8 Hz), 7.46 (s, 1H, quinoxaline-H_5), 7.78 (d, 2H, Ar–$H_{2,6}$, J = 8 Hz), 8.15 (d, 2H, Ar–$H_{3,5}$, J = 8 Hz), 8.31 (d, 1H, quinoxaline-H_8, J = 8 Hz), 11.46, 11.57 (2 s, 2NH, D_2O exchangeable). ^{13}C NMR (DMSO-d_6) δ (ppm): 29.11 (CH_2), 31.28 (CH_2), 122.75, 122.83, 126.37, 127.32, 127.67, 128.11, 131.28, 131.75, 133.14, 134.95, 142.36, 143.04, 144.11 (13 Ar–C), 163.04, 164.11 (2C=O). MS m/z: 372.11 (37.12%, M$^+$), 374.03 (12.53%, M^{+2}), 89.07 (100). Anal. calcd for: $C_{17}H_{13}ClN_4O_4$ (372.76): C, 54.78; H, 3.52; N, 15.03%, found: C, 54.33; H, 3.83; N, 15.43%.

Open Access Article. Published on 31 October 2023. Downloaded on 10/24/2025 6:18:49 PM.
This article is licensed under a Creative Commons Attribution-NonCommercial 3.0 Unported Licence.

4.2.7 3-(6-Chloro-1,2-dihydro-2-oxoquinoxalin-3-yl)-*N*-*p*-tolylpropanamide (11). Black powder; yield (65%); mp. 128–130 °C; IR (KBr, cm^{-1}): 3367, 3178 (2NH), 1689, 1666 (2C=O); ^{1}H NMR (400 MHz, DMSO-d_6) δ (ppm): 1.74 (t, 2H, CH_2x, J = 6.4 Hz), 2.32 (t, 2H, CH_2y, J = 6.4 Hz), 2.40 (s, 3H, CH_3), 7.02 (d, 2H, Ar–$H_{3,5}$, J = 8.4 Hz), 7.22 (s, 1H, quinoxaline-H_5), 7.49 (d, 1H, quinoxaline-H_7, J = 8.4 Hz), 7.68 (d, 2H, Ar–$H_{2,6}$, J = 8.4 Hz), 8.03 (d, 1H, quinoxaline-H_8, J = 8.4 Hz), 11.74, 11.86 (2 s, 2NH, D_2O exchangeable). ^{13}C NMR (DMSO-d_6) δ (ppm): 24.55 (CH_3), 29.75 (CH_2), 31.19 (CH_2), 123.52, 126.25, 126.44, 127.59, 130.55, 130.63, 130.67, 131.83, 132.23, 133.26, 134.26, 151.10, 151.15 (13 Ar–C), 164.44, 172.17 (2C=O). MS *m*/*z*: 341.25 (8.04%, M^+), 343.09 (2.66%, M^{+2}), 87.24 (100). Anal. calcd for: $C_{18}H_{16}ClN_3O_2$ (341.79): C, 63.25; H, 4.72; N, 12.29%, found: C, 63.66; H, 4.31; N, 12.53%.

4.2.8 3-(6-Chloro-1,2-dihydro-2-oxoquinoxalin-3-yl)-*N*-*m*-tolylpropanamide (12). Pale brown powder; yield (70%); mp. 150–152 °C; IR (KBr, cm^{-1}): 3340, 3184 (2NH), 1690, 1630 (2C=O); ^{1}H NMR (400 MHz, DMSO-d_6) δ (ppm): 1.72 (t, 2H, CH_2x, J = 8 Hz), 2.32 (t, 2H, CH_2y, J = 8 Hz), 2.41 (s, 3H, CH_3), 6.65 (d, 1H, Ar–H_4, J = 8 Hz), 7.21 (t, 1H, Ar–H_5, J = 7.6 Hz), 7.49 (d, 1H, quinoxaline-H_7, J = 8.4 Hz), 7.71 (s, 1H, Ar–H_2), 7.82 (d, 1H, Ar–H_6, J = 8 Hz), 7.96 (s, 1H, quinoxaline-H_5), 8.09 (d, 1H, quinoxaline-H_8, J = 8.4 Hz), 11.20, 11.21 (2 s, 2NH, D_2O exchangeable). ^{13}C NMR (DMSO-d_6) δ (ppm): 24.17 (CH_3), 29.30 (CH_2), 31.26 (CH_2), 123.52, 126.23, 126.43, 127.59, 130.43, 130.54, 130.97, 131.51, 132.10, 132.15, 134.31, 151.29, 151.31 (13 Ar–C), 164.15, 172.24 (2C=O). MS *m*/*z*: 341.12 (9.03%, M^+), 343.40 (2.98%, M^{+2}), 87.15 (100). Anal. calcd for: $C_{18}H_{16}ClN_3O_2$ (341.79): C, 63.25; H, 4.72; N, 12.29%, found: C, 63.71; H, 4.45; N, 12.66%.

4.2.9 3-(6-Chloro-1,2-dihydro-2-oxoquinoxalin-3-yl)-*N*-*o*-tolylpropanamide (13). Dark brown powder; yield (69%); mp. 138–140 °C; IR (KBr, cm^{-1}): 3360, 3250 (2NH), 1693, 1633 (2C=O); ^{1}H NMR (400 MHz, DMSO-d_6) δ (ppm): 1.73 (t, 2H, CH_2x, J = 8 Hz), 2.32 (t, 2H, CH_2y, J = 8 Hz), 2.40 (s, 3H, CH_3), 6.77 (t, 1H, Ar–H_4, J = 8 Hz), 7.83 (d, 1H, Ar–H_3, J = 8.4 Hz), 7.07 (t, 1H, Ar–H_5, J = 8.4 Hz), 7.13 (d, 1H, quinoxaline-H_7, J = 8.4 Hz), 7.50 (d, 1H, Ar–H 6, J = 8.4 Hz), 7.53 (s, 1H, quinoxaline-H_5), 8.26 (d, 1H, quinoxaline-H_8, J = 8.4 Hz), 11.67, 11.77 (2s, 2NH, D_2O exchangeable). ^{13}C NMR (DMSO-d_6) δ (ppm): 24.90 (CH_3), 29.37 (CH_2), 31.46 (CH_2), 123.24, 124.35, 128.03, 129.40, 129.47, 129.60, 134.20, 134.40, 135.47, 135.60, 135.78, 137.40, 137.49 (13 Ar–C), 164.60, 168.78 (2C=O). MS *m*/*z*: 341.28 (17.51%, M^+), 343.20 (5.88%, M^{+2}), 87.04 (100). Anal. calcd for: $C_{18}H_{16}ClN_3O_2$ (341.79): C, 63.25; H, 4.72; N, 12.29%, found: C, 63.55; H, 4.31; N, 12.44%.

4.2.10 3-(6-Chloro-1,2-dihydro-2-oxoquinoxalin-3-yl)-*N*-(4-methoxyphenyl) propanamide (14). Light brown powder; yield (76%); mp. 242–245 °C; IR (KBr, cm^{-1}): 3345, 3167 (2NH), 1679, 1638 (2C=O); ^{1}H NMR (400 MHz, DMSO-d_6) δ (ppm): 1.77 (t, 2H, CH_2x, J = 8 Hz), 2.38 (t, 2H, CH_2y, J = 8 Hz), 3.90 (s, 3H, OCH_3), 7.22 (d, 2H, Ar–$H_{3,5}$, J = 8.4 Hz), 7.70 (d, 1H, quinoxaline-H_7, J = 8.4 Hz), 7.82 (s, 1H, quinoxaline-H_5), 7.97 (d, 2H, Ar–$H_{2,6}$, J = 8.4 Hz), 8.46 (d, 1H, quinoxaline-H_8, J = 8.4 Hz), 11.77, 11.87 (2s, 2NH, D_2O exchangeable). ^{13}C NMR (DMSO-d_6) δ (ppm): 29.10 (CH_2), 31.15 (CH_2), 55.39 (OCH_3), 118.22, 119.67, 120.10, 120.46, 128.22, 128.82, 130.35, 131.15, 131.68, 132.01, 134.26, 145.03, 145.05 (13 Ar–C), 168.93, 170.68 (2C=O). MS *m*/*z*: 357.01 (12.03%, M^+), 359.40 (4.11%, M^{+2}), 82.17 (100). Anal. calcd for: $C_{18}H_{16}ClN_3O_3$ (357.79): C, 60.42; H, 4.51; N, 11.74%, found: C, 60.71; H, 4.82; N, 11.52%.

4.2.11 *N*-(4-Acetylphenyl)-3-(6-chloro-1,2-dihydro-2-oxoquinoxalin-3-yl) propanamide (15). Black powder; yield (62%); mp. 180–182 °C; IR (KBr, cm^{-1}): 3373, 3260 (2NH), 1716, 1673, 1642 (3C=O); ^{1}H NMR (400 MHz, DMSO-d_6) δ (ppm): 1.65 (t, 2H, CH_2x, J = 8 Hz), 2.35 (t, 2H, CH_2y, J = 8 Hz), 2.67 (s, 3H, $COCH_3$), 7.21 (d, 1H, quinoxaline-H_7, J = 8 Hz), 7.42 (d, 1H, quinoxaline-H_8, J = 8 Hz), 7.47 (s, 1H, quinoxaline-H_5), 7.76 (d, 2H, Ar–H 2,6, J = 8 Hz), 8.00 (d, 2H, Ar–$H_{3,5}$, J = 8 Hz), 12.23, 12.37 (2 s, 2NH, D_2O exchangeable). ^{13}C NMR (DMSO-d_6) δ (ppm): 28.22 (CO CH_3), 29.82 (CH_2), 31.15 (CH_2), 118.03, 119.05, 120.19, 120.20, 128.39, 128.67, 130.10, 131.01, 131.26, 132.18, 134.22, 145.46, 145.55, (13 Ar–C), 167.35, 171.15 and 188.93 (3C=O). MS *m*/*z*: 369.13 (39.02%, M^+), 371.17 (12.98%, M^{+2}), 82.29 (100). Anal. calcd for: $C_{19}H_{16}ClN_3O_3$ (369): C, 61.71; H, 4.36; N, 11.36%, found: C, 61.35; H, 4.62; N, 11.68%.

4.2.12 4-(3-(6-Chloro-1,2-dihydro-2-oxoquinoxalin-3-yl) propanamido)benzoic acid (16). Brown powder; yield (75%); mp. 133–135 °C; IR (KBr, cm^{-1}): 3406–2620 (br, OH), 3221, 3137 (2NH), 1700, 1688, 1654 (3C=O); ^{1}H NMR (400 MHz, DMSO-d_6) δ (ppm): 1.62 (t, 2H, CH_2x, J = 7.6 Hz), 2.24 (t, 2H, CH_2y, J = 7.6 Hz), 7.27 (d, 1H, quinoxaline-H_7, J = 8 Hz), 7.43 (d, 1H, quinoxaline-H_8, J = 8 Hz), 7.47 (s, 1H, quinoxaline-H_5), 7.97 (d, 2H, Ar–$H_{2,6}$, J = 8 Hz), 8.46 (d, 2H, Ar–H 3,5, J = 8 Hz), 10.83 (s, 1H, COOH), 12.75, 12.82 (br, 2NH, D_2O exchangeable). ^{13}C NMR (DMSO-d_6) δ (ppm): 29.95 (CH_2), 31.61 (CH_2), 123.21, 125.24, 126.92, 127.30, 127.31, 127.50, 128.23, 129.66, 130.05, 130.80, 131.26, 131.27, 132.56 (13 Ar–C), 166.21, 169.31, 171.93 (3C=O). MS *m*/*z*: 371.37 (45.11%, M^+), 373.17 (15.07%, M^{+2}), 84.19 (100). Anal. calcd for: $C_{18}H_{14}ClN_3O_4$ (371.77): C, 58.15; H, 3.80; N, 11.30%, found: C, 58.46; H, 3.43; N, 11.63%.

4.2.13 Ethyl 4-(3-(6-chloro-1,2-dihydro-2-oxoquinoxalin-3-yl) propanamido) benzoate (17). Pale brown powder; yield (61%); mp. 120–122 °C; IR (KBr, cm^{-1}): 3367, 3230 (2NH), 1745, 1693, 1654 (3C=O); 1 H NMR (400 MHz, DMSO-d_6) δ (ppm): 1.34 (t, 3H, OCH_2CH_3, J = 7.2 Hz),1.73 (t, 2H, CH_2x, J = 7.2 Hz), 2.34 (t, 2H, CH_2y, J = 7.2 Hz), 4.36 (q, 2H, OCH_2CH_3, J = 7.2 Hz), 6.47 (d, 1H, quinoxaline-H_7, J = 8.4 Hz), 7.41 (d, 1H, quinoxaline-H_8, J = 8.4 Hz), 7.49 (d, 2H, Ar–$H_{2,6}$, J = 8.4 Hz), 7.94 (s, 1H, quinoxaline-H_5), 8.09 (d, 2H, Ar–H 3,5, J = 8.4 Hz), 11.89, 11.92 (2s, 2NH, D_2O exchangeable). ^{13}C NMR (DMSO-d_6) δ (ppm): 14.11 (CH_3), 29.40 (CH_2), 31.49 (CH_2), 60.03 (OCH_2CH_3), 117.91, 118.03, 128.24, 129.40, 129.47, 129.60, 134.11, 134.12, 135.13, 135.38, 135.39, 137.78, 137.90 (13 Ar–C), 164.07, 168.16 (2C=O of amide), 172.39 (C=O of ester). MS *m*/*z*: 399.06 (62.14%, M^+), 401.19 (20.94%, M^{+2}), 88.13 (100). Anal. calcd for: $C_{20}H_{18}ClN_3O_4$ (399.83): C, 60.08; H, 4.54; N, 10.51%, found: C, 60.41; H, 4.71; N, 10.77%.

4.2.14 2,4-Dichloro-*N*′-(3-(6-chloro-3-oxo-3,4-dihydroquinoxalin-2-yl)-propanoyl) benzohydrazide (19). A solution of acid hydrazide, **18** (2.66 g, 0.01 mol) was treated with 2,4-dichlorobenzoyl chloride (2.09 g, 0.01 mol) in 20 ml ethanol

 © 2023 The Author(s). Published by the Royal Society of Chemistry

Open Access Article. Published on 31 October 2023. Downloaded on 10/24/2025 6:18:49 PM. This article is licensed under a Creative Commons Attribution-NonCommercial 3.0 Unported Licence.

with a little amount of DMF. The reaction mixture was heated under reflux for 4 h, and then allowed to cool down. The final compound **19** was obtained after filtration and crystallization from ethanol. Brown powder; yield (51%); mp. 188–190 °C; IR (KBr, cm^{-1}): 3274, 3211 and 3107 (3NH), 1700, 1688, 1617 (3C=O); ^{1}H NMR (400 MHz, DMSO-d_6) δ (ppm): 2.74 (t, 2H, CH_2, $J = 4$ Hz), 3.09 (t, 2H, CH_2, $J = 4$ Hz), 6.86 (s, 1H, quinoxaline-H_5), 6.98 (d, 1H, quinoxaline-H_7, $J = 4$ Hz), 7.28 (d, 1H, Ar–H_5, $J = 8$ Hz), 7.43 (s, 1H, Ar–H_3), 7.62 (d, 1H, quinoxaline-H_8, $J = 8$ Hz), 7.80 (d, 1H, Ar–H_6, $J = 8$ Hz), 12.42, 12.43 and 12.60 (s, 3NH, D_2O exchangeable). ^{13}C NMR (DMSO-d_6) δ (ppm): 29.75 (CH_2), 31.02 (CH_2), 119.12, 120.19, 120.67, 120.92, 125.45, 125.75, 126.12, 126.19, 126.67, 128.34, 129.50, 130.57, 131.02, 162.70, 167.67, 170.34 (3C=O). MS *m*/*z* (%): 438 (20.41, M^+), 440.86 (6.5, M^{+2}), 185.91 (100). Anal. calcd for: $C_{18}H_{13}N_4O_3Cl_3$ (438): C, 49.17; H, 2.98; N, 12.74; Cl, 24.19%, found: C, 49.52; H, 2.48; N, 12.43; Cl, 24.55%.

4.2.15 4-(3-(6-Chloro-1,2-dihydro-2-oxoquinoxalin-3-yl) propaneamido)-4-oxobutanoic acid (20). Compound **18** (2.66 g, 0.01 mol) was heated under reflux in 20 ml ethanol in presence of catalytic quantity of DMF with an equivalent amount of succinic anhydride (1.00 g, 0.01 mol). The reaction was cooled after 3 h of refluxing. After that, compound **20** was produced by collecting the raw powder and recrystallizing it from ethanol. Black powder; yield (72%); mp. 320–322 °C; IR (KBr, cm^{-1}): 3360 (br., OH), 3337, 3293 and 3131 (3NH), 1706, 1689, 1665 and 1617 (4C=O); ^{1}H NMR (400 MHz, DMSO- d_6) δ (ppm): 2.38 (t, 2H, CH_2CH_2COOH), 2.59 (t, 2H, CH_2CH_2COOH, $J = 4$ Hz), 2.64 (t, 2H, CH_2, $J = 4$ Hz), 3.04 (t, 2H, CH_2, $J = 4$ Hz), 7.30 (d, 1H, quinoxaline-H_7, $J = 8$ Hz), 7.33 (s, 1H, quinoxaline-H_5), 7.75 (d, 1H, quinoxaline-H_8, $J = 8$ Hz), 10.85 (s, OH, D_2O exchangeable), 12.38, 12.40 and 12.41 (s, 3NH, D_2O exchangeable). ^{13}C NMR (DMSO-d_6) δ (ppm): 29.40 (CH_2), 31.14 (CH_2), 32.47 (CH_2), 32.68 (CH_2), 120.74, 121.01, 121.27, 124.13, 124.46, 131.20, 131.96, 161.13, 166.65, 167.04, 167.31 (4C=O). MS *m*/*z* (%): 366 (14.41, M^+), 368 (4.56, M^{+2}), 185.02 (100). Anal. calcd for: $C_{15}H_{15}N_4O_5Cl$ (366): C, 49.12; H, 4.12; N, 15.28; Cl, 9.67%, found: C, 49.53; H, 4.37; N, 15.71; Cl, 9.32%.

4.2.16 2-(2-(3-(6-Chloro-3-oxo-3,4-dihydroquinoxalin-2-yl) propanoyl)hydrazine-1-carbonyl) benzoic acid (21). An equimolar quantities of acid hydrazide, **18** (2.66 g, 0.01 mol) and phthalic anhydride (1.48 g, 0.01 mol) were heated under reflux in 20 ml ethanol with a catalytic quantity of DMF. The reaction was continued for 4 h and allowed to cool. The target compound **21** was attained by filtration and crystallization from ethanol. Light brown powder; yield (81%); mp. 218–220 °C; IR (KBr, cm^{-1}): 3339 (br., OH), 3267, 3206 and 3142 (3NH), 1705, 1689, 1662, 1624 (4C=O); ^{1}H NMR (400 MHz, DMSO-d_6) δ (ppm): 2.85 (t, 2H, CH_2, $J = 4$ Hz), 3.09 (t, 2H, CH_2, $J = 4$ Hz), 6.84 (s, 1H, quinoxaline-H_5), 6.94 (d, 1H, quinoxaline-H_7, $J = 8$ Hz), 7.28 (d, 1H, quinoxaline-H_8, $J = 8$ Hz), 7.44 (t, 1H, Ar–H_4, $J = 12$ Hz), 7.57 (t, 1H, Ar–H_5, $J = 12$ Hz), 8.20 (d, 1H, Ar–H_6, $J = 8$ Hz), 8.74 (d, 1H, Ar–H_3, $J = 8$ Hz), 10.80 (s, OH, D_2O exchangeable), 12.43, 12.44 and 12.83 (s, 3NH, D_2O exchangeable). ^{13}C NMR (DMSO-d_6) δ (ppm): 29.66 (CH_2), 31.95 (CH_2), 110.45, 112.32, 117.36, 119.70, 120.73, 121.26, 124.45, 131.95, 139.66, 140.57, 142.43, 142.87, 151.11, 161.11, 168.88, 170.26 and 173.45 (4C=O). MS *m*/*z* (%): 414 (20.41, M^+), 416.06 (6.5, M^{+2}), 184.91 (100). Anal. calcd for: $C_{19}H_{15}N_4O_5Cl$ (414): C, 55.02; H, 3.64; N, 13.51; Cl, 8.55%, found: C, 55.41; H, 3.22; N, 13.82; Cl, 8.16%.

4.2.17 3-(6-Chloro-1,2-dihydro-2-oxoquinoxalin-3-yl)-*N*-(1,3-dioxoisoindolin-2-yl) propanamide (22). The intermediate **18** (2.66 g, 0.01 mol) was mixed with an equivalent amount of phthalic anhydride (1.48 g, 0.01 mol) in 20 ml of glacial acetic acid with a catalytic amount of DMF. The reaction was heated under reflux for 4 h, and the resulting product was filtered before being recrystallized from the ethanol to afford compound **22**.

4.3 Another procedure

Compound **21** (0.01 mol) was refluxed in 15 ml of glacial acetic acid for 2 h, and the resulting product was filtered and recrystallized from the ethanol to afford compound **22**. Light brown powder; yield (78%); mp. 264–266 °C; IR (KBr, cm^{-1}): 3327 and 3189 (2 NH), 1751, 1669, 1635 and 1623 (4C=O); ^{1}H NMR (400 Mz, DMSO-d_6) δ (ppm): 2.82 (t, 2H, CH_2, $J = 4$), 3.03 (t, 2H, CH_2, $J = 4$ Hz), 6.89 (s, 1H, quinoxaline-H_5), 6.97 (d, 1H, quinoxaline-H_7, $J = 8$ Hz), 7.32 (d, 1H, quinoxaline-H_8, $J = 8$ Hz), 7.48 (t, 1H, Ar–H_4, $J = 8$ Hz), 7.60 (t, 1H, Ar–H_5, $J = 8$ Hz), 8.28 (d, 1H, Ar–H_6, $J = 8$ Hz), 8.78 (d, 1H, Ar–H_3, $J = 8$ Hz), 12.22 and 12.54 (s, 2NH, D_2O exchangeable). ^{13}C NMR (DMSO-d_6) δ (ppm): 29.33 (CH_2), 31.54 (CH_2), 115.66, 115.72, 115.85, 115.94, 117.59, 119.53, 120.41, 121.23, 121.31, 124.07, 131.38, 135.81, 135.84 (13 Ar–C), 159.68, 165.73, 166.70 and 169.74 (4C=O). MS *m*/*z* (%): 396 (9.05, M^+), 398.52 (2.98, M^{+2}), 102.34 (100). Anal. calcd for: $C_{19}H_{13}N_4O_4Cl$ (396): C, 57.51; H, 3.30; N, 14.12; Cl, 8.94%, found: C, 57.04; H, 3.72; N, 14.43; Cl, 8.56%.

4.4. Biological evaluation

Antiproliferative assay: the prepared compounds were estimated for their antiproliferative activity against two human breast cancer cell lines, MCF-7 and HCT-116 in comparison with doxorubicin as a reference standard at concentrations 100, 50, 25, 12.5, 6.25, 3.125, and 1.56 μM utilizing MTT assay guided by the reported procedure.[33]

VEGFR-2 inhibition estimation: VEGFR-2 inhibition estimation was executed utilizing VEGFR-2 (KDR) Kinase Assay Kit of Biosciences and the IC50 values were detected according to the manufacturer's instructions and the reported method.[37]

Quantitative determination of $VEGFR_2$ in MCF-7 cell line: ELISA analysis to determine $VEGFR_2$ quantitatively in MCF-7 cell line is following the reported procedure[38]

Effect of 14 on angiogenesis (VEFG-A) level: ELISA analysis to determine VEGF-A secretion is following the reported procedure.[40]

Cell cycle analysis: FACS Caliber flow cytometer was utilized to determine the effect of **14** on the cell cycle of breast tumor NCF-7 guided by the previously reported method.[39]

Annexin-V-FITC apoptosis assay: the apoptosis of **14** was detected through Annexin V-FITC/PI apoptosis detection kit utilizing FACS Caliber flow cytometer following the reported procedure.[40]

Open Access Article. Published on 31 October 2023. Downloaded on 10/24/2025 6:18:49 PM.
This article is licensed under a Creative Commons Attribution-NonCommercial 3.0 Unported Licence.

Effect of **14** on active caspase-3 level

Caspase-3 is evaluated by using the reported method.[41]

Evaluation of apoptosis regulator p53

P53 expression is measured in MCF-7 by the reported method.[42]

Evaluation of BAX and BCL2 levels[43,44]

Author contributions

Magda M. F. Ismail (corresponding author)-conceived and designed the analysis and wrote the article, Taghreed Z. Shawer-revised the manuscript and collected the data, Rabab S. Ibrahim-performed the synthetic work and collected the data, Mostafa S. Abusaif-contributed in synthetic part, Mona M. Kamal-contributed data and analysis, Rasha M. Allam-performed some analysis, Yousry A. Ammar-designed the chemistry part and revised the manuscript.

Conflicts of interest

The authors declare that they have no conflicts of interest. The authors alone are responsible for the content and writing of this manuscript.

References

1 L. Zhao, H. Y. Chen, L. Lu, L. Wang, X. K. Zhang and X. L. Guo, New insights into the role of co-receptor neuropilins in tumour angiogenesis and lymphangiogenesis and targeted therapy strategies, *J. Drug Targeting*, 2021, **29**, 155–167.

2 C. B. Prasad, D. Singh, L. K. Pandey, S. Pradhan, S. Singh and G. Narayan, VEGFa/VEGFR2 autocrine and paracrine signaling promotes cervical carcinogenesis *via* β-catenin and snail, *Int. J. Biochem. Cell Biol.*, 2022, **142**, 106122.

3 Y. Liu, L. Yang, Y. Wang, C. Lin, D. Zhang, J. Chen, L. Ouyang, F. Wu, J. Zhang and C. Lei, Recent progress on vascular endothelial growth factor receptor inhibitors with dual targeting capabilities for tumor therapy, *J. Hematol. Oncol.*, 2022, **15**, 89, DOI: 10.1186/s13045-022-01310-7.

4 C. C. Estrada, A. Maldonado and S. K. Mallipattu, Therapeutic inhibition of VEGF signaling and associated nephrotoxicities, *J. Am. Soc. Nephrol.*, 2019, **30**, 187–200.

5 P. Zhu, C. Hu, K. Hui and X. Jiang, The role and significance of VEGFR2 regulatory T cells in tumor immunity, *OncoTargets Ther.*, 2017, **10**, 4315–4319.

6 F. Gao and C. Yang, Anti-VEGF/VEGFR2 monoclonal antibodies and their combinations with PD-1/PD-L1 inhibitors in clinic, *Curr. Cancer Drug Targets*, 2020, **20**, 3–18.

7 R. Jr Roskoski, Vascular endothelial growth factor (VEGF) and VEGF receptor inhibitors in the treatment of renal cell carcinomas, *Pharmacol. Res.*, 2017, **120**, 116–132.

8 M. Yousefian and R. Ghodsi, Structure–activity relationship studies of indolin-2-one derivatives as vascular endothelial growth factor receptor inhibitors and anticancer agents, *Arch. Pharm.*, 2020, **353**, e2000022, DOI: 10.1002/ardp.202000022.

9 K. K. Bhanumathy, A. Balagopal, F. S. Vizeacoumar, F. J. Vizeacoumar, A. Freywald and V. Giambra, Protein tyrosine kinases: their roles and their targeting in leukemia, *Cancers*, 2021, **13**(2), 184, DOI: 10.3390/cancers13020184.

10 M. Liao, J. Zhang, G. Wang, L. Wang, J. Liu, L. Ouyang and B. Liu, Small-moleculedrug discovery in triple negative breast cancer: current situation and future directions, *J. Med. Chem.*, 2021, **64**, 2382–2418.

11 S. T. Staben, J. A. Feng, K. Lyle, M. Belvin, J. Boggs, J. D. Burch, C. C. Chua, H. Cui, A. G. DiPasquale, L. S. Friedman, C. Heise, H. Koeppen, A. Kotey, R. Mintzer, A. Oh, D. A. Roberts, L. Rouge, J. Rudolph, C. Tam, W. Wang, Y. Xiao, A. Young, Y. Zhang and K. P. Hoeflich, Back pocket flexibility provides group II p21-activated kinase (PAK) selectivity for type I 1/2 kinase inhibitors, *J. Med. Chem.*, 2014, **57**, 1033–1045.

12 A. Abdeldayem, Y. S. Raouf, S. N. Constantinescu, R. Moriggl and P. T. Gunning, Advances in covalent kinase inhibitors, *Chem. Soc. Rev.*, 2020, **49**, 2617–2687.

13 M. M. Alanazi, H. Elkady, N. A. Alsaif, A. J. Obaidullah, H. M. Alkahtani, M. M. Alanazi, M. A. Alharbi, I. H. Eissa and M. A. Dahab, New quinoxaline-based VEGFR-2 inhibitors: design, synthesis, and antiproliferative evaluation with *in silico* docking, ADMET, toxicity, and DFT studies, *RSC Adv.*, 2021, **11**, 30315.

14 M. Montana, V. Montero, O. Khoumeri and P. Vanelle, *Molecules*, 2020, **25**, 2784.

15 M. Montana, F. Mathias, T. Terme and P. Vanelle, *Eur. J. Med. Chem.*, 2019, **163**, 136–147.

16 E. M. Abbass, A. K. Khalil, M. M. Mohamed, I. H. Eissa and A. M. El-Naggar, *Bioorg. Chem.*, 2020, **104**, 104255.

17 M. A. Naylor, M. A. Stephens, J. Nolan, B. Sutton, J. H. Tocher, E. M. Fielden, G. E. Adams and I. J. Stratford, *Anti-Cancer Drug Des.*, 1993, **8**, 439–461.

18 T. H. Corbett, P. Lorusso, L. Demchick, C. Simpson, S. L. Pugh, K. White, J. Kushner, L. L. Polin, J. A. Meyer, J. Czarnecki, L. K. Heilbrun, J. P. Horwitz, J. L. Gross, C. H. Behrens, B. A. Harrison, R. J. Mcripley and G. L. Trainor, *Invest. New Drugs*, 2004, **16**, 129–139.

19 M. M. F. Ismail, D. H. Soliman, A. M. Farrag and R. Sabour, Synthesis, antitumor activity, pharmacophore modeling and QSAR studies of novel pyrazoles and pyrazolo [1, 5-*a*] pyrimidines against breast adenocarcinoma mcf-7 cell line, *Int. J. Pharm. Pharm. Sci.*, 2016, **8**, 434–442.

20 M. M. F. Ismail, D. H. Soliman, R. Sabour and A. M. Farrag, Synthesis of new arylazopyrazoles as apoptosis inducers: Candidates to inhibit proliferation of MCF-7 cells, *Arch. Pharm.*, 2020, **354**, 2000214, DOI: 10.1002/ardp.202000214.

21 M. M. F. Ismail, A. M. Farrag and M. F. Harras, Novel 1,3,4-Triaryl Pyrazoles: Synthesis, QSAR Studies and Cytotoxicity against Breast Cancer, *Anti-Cancer Agents Med. Chem.*, 2019, **19**, 948–959.

22 M. M. F. Ismail, H. S. El-Zahabi, R. S. Ibrahim and A. B. Mehany, Design and synthesis of novel tranilast analogs: Docking, antiproliferative evaluation and *in-silico*

 © 2023 The Author(s). Published by the Royal Society of Chemistry

Open Access Article. Published on 31 October 2023. Downloaded on 10/24/2025 6:18:49 PM.
This article is licensed under a Creative Commons Attribution-NonCommercial 3.0 Unported Licence.

screening of TGFβR1 inhibitors, *Bioorg. Chem.*, 2020, **105**, 104368, DOI: 10.1016/j.bioorg.2020.104368.

23 A. M. Farrag, M. H. Ibrahim, A. B. Mehany and M. M. F. Ismail, New cyanopyridine-based scaffold as PIM-1 inhibitors and apoptotic inducers: Synthesis and SARs study, *Bioorg. Chem.*, 2020, **105**, 104378.

24 M. M. F. Ismail, A. M. Farrag, M. F. Harras, M. H. Ibrahim and A. B. Mehany, Apoptosis: A target for anticancer therapy with novel cyanopyridines, *Bioorg. Chem.*, 2020, **94**, 103481.

25 A. M Farrag, M. F Harras and M. M. F. Ismail, Design, Synthesis and QSAR Studies of Novel 1,3,4-Triarylpyrazoles as Anti-breast Cancer Agents, *J. Appl. Pharm. Sci.*, 2017, **3**(1), 63–74.

26 M. M. F. Ismail, A. M. Farrag and D. Abou-El Ella, Synthesis, anticancer screening, and *in silico* ADME prediction of novel 2-pyridones as Pim inhibitors, *J. Heterocycl. Chem.*, 2020, **57**, 1–19, DOI: 10.1002/jhet.4064.

27 S. Tariq, O. Alam and M. Amir, Synthesis, anti-inflammatory, p38α MAP kinase inhibitory activities and molecular docking studies of quinoxaline derivatives containing triazole moiety, *Bioorg. Chem.*, 2018, **76**, 343–358, DOI: 10.1016/j.bioorg.2017.12.003.

28 https://www.masterorganicchemistry.com/reaction-guide/formation-of-amides-from-esters/Biology.

29 Y. A. Ammar, M. M. F. Ismail, M. K. Ibrahim and H. S. A. El-Zahaby, 3-ethoxycarbonylmethylenequinoxalin-2-one in heterocyclic synthesis. Part1: synthesis of new substituted and condensed quinoxalines, *Afinidad*, 2005, **516**, 151.

30 S. El-Hashash, A. Maher, D. B. Guirguis, N. A. M. AbdEl-Wahed and M. A. Kadhim, Synthesis of novel series of phthalazine derivatives with antibacterial and mantifungal evaluation, *J. Chem. Eng. Process Technol.*, 2014, **5**(4), 1000191–1000196.

31 L. A. Shemchuk, V. P. Chernykh, P. S. Arzumanov and I. L. Starchikova, Synthesis of 3-amino-3, 4-dihydroquinazolin-4-one derivatives from anthranilic acid hydrazide and dicarboxylic acids, *Russ. J. Org. Chem.*, 2007, **43**(12), 1830–1835.

32 H. El-Sabbagh, I. Osama, M. E. El-Sadek, S. M. Lashine, S. H. Yassin and S. M. El-Nabtity, Synthesis of new 2 (1H)-quinoxalinone derivatives for antimicrobial and anti-inflammatory evaluation, *Med. Chem. Res.*, 2009, **18**(9), 782–797.

33 L. Freimoser, C. A. Jakob, M. Aebi and U. Tuor, *Appl. Environ. Microbiol.*, 1999, **65**(8), 3727–3729.

34 T. H. Yang, C. I. Lee, W. H. Huang and A. R. Lee, Synthesis and evaluation of novel 2-pyrrolidone-fused (2-oxoindolin-3-ylidene) methylpyrrole derivatives as potential multi-target tyrosine kinase receptor inhibitors, *Molecules*, 2017, **22**(6), 913.

35 M. A. Abdelgawad, A. M. Hayallah, S. N. A. Bukhari, A. Musa, M. Elmowafy, H. M. Abdel-Rahman and K. Mohammed, Design, Synthesis, Molecular Modeling, and Anticancer Evaluation of New VEGFR-2 Inhibitors Based on the Indolin-2-One Scaffold, *Pharma*, 2022, **15**(11), 1416.

36 A. Shindikar, G. Deshpande, U. Chaudhari, D. Bhatia and K. Joshi, Comparative effect of tyrosine kinase inhibitors in human cancer cell lines, *J. Pharm. Clin. Res.*, 2016, **1**(2), 555557.

37 VEGFR-2 (KDR), kinase assay kit catalog, 40325, https://bpsbioscience.com/.

38 T. Atakul, serum levels of angiogenic factors distinguish between women with preeclampsia and normotensive pregnant women but not severity of preeclampsia in an obstetric center in Turkey, *Med. Sci. Monit.*, 2019, **25**, 6935–6942, DOI: 10.12659/MSM.915092.

39 P. Mabeta and V. Steenkamp, The VEGF/VEGFR Axis Revisited: implications for cancer therapy, *Int. J. Mol. Sci.*, 2022, **23**, 15585, DOI: 10.3390/ijms232415585.

40 B. Y. Jeong, K. H. Cho, K. J. Jeong, Y. Y. Park, J. M. Kim, S. Y. Rha, C. G. Park, G. B. Mills, J. H. Cheong and H. Y. Lee, Rab25 augments cancer cell invasiveness through a β1 integrin/EGFR/VEGF-A/Snail signaling axis and expression of fascin, *Exp. Mol. Med.*, 2018, **50**, e435, DOI: 10.1038/emm.2017.248.

41 Y. Wang, P. Ji, J. Liu, R. R. Broaddus, F. Xue and W. Zhang, *Mol. Cancer*, 2009, **8**, 8, DOI: 10.1186/1476-4598-8-8.

42 S. Elmore, *Toxicol. Pathol.*, 2007, **35**, 495–516, DOI: 10.1080/01926230701320337.

43 P. J. Lakshmi, B. V. S. S. Kumar, R. S. Nayana, M. S. Mohan, R. Bolligarl, S. K. Das, M. U. Bhanu, A. K. Kondapi and M. Ravikumar, Design, synthesis, and discovery of novel non-peptide inhibitor of Caspase-3 using ligand based and structure based virtual screening approach, *Bioorg. Med. Chem.*, 2009, **17**, 6040–6047.

44 J. T. Zilfou and S. W. Lowe, Tumor suppressive functions of p53, *Cold Spring Harb. Perspect. Biol.*, 2009, **1**(5), 001883, DOI: 10.1101/cshperspect.a001883.

45 S. Fulda, L. Galluzzi and G. Kroemer, *Nat. Rev. Drug Discovery*, 2010, **9**, 447–464.

46 S. Salakou, D. Kardamakis, A. C. Tsamandas, V. Zolota, E. Apostolakis, V. Tzelepi, P. Papathanasopoulos, D. S. Bonikos, T. Papapetropoulos and T. Petsas, Increased Bax/Bcl-2 Ratio Up-regulates Caspase-3 and Increases Apoptosis in the Thymus of Patients with Myasthenia Gravis, *In Vivo*, 2007, **21**, 123–132.

47 D. Antoine, M. Olivier and Z. Vincent, SwissADME: a free web tool to evaluate pharmacokinetics, drug likeness and medicinal chemistry friendliness of small molecules, *Sci. Rep.*, 2017, **7**(1), 42717.

48 A. L. Christopher, L. Franco, W. D. Beryl and J. F. Paul, Experimental and computational approaches to estimate solubility and permeability in drug discovery and development settings, *Adv. Drug Delivery Rev.*, 1997, **23**, 3–25.

49 D. F. Veber, S. R. Johnson, H. Y. Cheng, B. R. Smith, K. W. Ward and K. D. Kopple, Molecular properties that influence the oral bioavailability of drug candidates, *J. Med. Chem.*, 2002, **45**(12), 2615–2623.

50 M. d. S. Marciane, C. Marina, S. D. Thiago, A. F. Mary, E. d. C. João, d. C. V. Maria and S. N. F. Anelise, Synthesis, Antiproliferative Activity and Molecular Properties

Open Access Article. Published on 31 October 2023. Downloaded on 10/24/2025 6:18:49 PM.
This article is licensed under a Creative Commons Attribution-NonCommercial 3.0 Unported Licence.

Predictions of Galloyl Derivatives, *Molecules*, 2015, **20**, 5360–5373.

51 S. Rampogu, A. Baek, A. Zeb and K. W. Lee, Exploration for novel inhibitors showing back-to-front approach against VEGFR-2 kinase domain (4AG8) employing molecular docking mechanism and molecular dynamics simulations, *BMC Cancer*, 2018, **18**(1), 1–21.

52 A. E. Abdallah, R. R. Mabrouk, M. M. S. Al Ward, S. I. Eissa, E. B. Elkaeed, A. B. Mehany and M. A. El-Zahabi, Synthesis, biological evaluation, and molecular docking of new series of antitumor and apoptosis inducers designed as VEGFR-2 inhibitors, *J. Enzyme Inhib. Med. Chem.*, 2022, **37**(1), 573–591.

 © 2023 The Author(s). Published by the Royal Society of Chemistry